Elsevier Editorial System(tm) for Engineering Failure Analysis
Manuscript Draft

Manuscript Number: EFA-D-14-00590

Title: Observing early stage rail axle bearing damage

Article Type: Special Issue : ICEFA VI

Keywords: Fatigue markings; Forensic engineering; Bearing failure; Railway engineering

Corresponding Author: Dr. Nicola Symonds,

Corresponding Author's Institution: University of Southampton

First Author: Nicola Symonds

Order of Authors: Nicola Symonds; Ilaria Corni; Robert Wood; Adam Wasenczuk; David Vincent

Abstract: A novel condition monitoring system has for the first time enabled reliable extraction from service and detailed forensic examination of failing rail axle bearings, before the usual catastrophic destruction of the evidence. Computed Tomography has been used to produce a map of the damage allowing targeted sectioning of subsurface cracking. Traditional metallographic techniques have revealed large white etched layers associated with the subsurface cracking, while observations with a scanning electron microscope have confirmed rolling contact fatigue crack propagation, possibly initiated from pre-existing electrical arcing damage of the raceways.

Suggested Reviewers:

University of Southampton,
Highfield Campus (B7),
Southampton,
SO17 1BJ
29 September 2014

Journal of Engineering Failure Analysis
Elsevier.

Dear Editor-in-Chief,

Re: Manuscript "Observing early stage rail axle bearing damage"

I hereby submit the above titled manuscript for your consideration to be included in the Special Edition of your journal covering the papers presented at the Sixth International Conference of Engineering Failure Analysis.

I look forward to your feedback.

Yours truly,

Nicola Symonds

N.Symonds@soton.ac.uk
07817000390

***Highlights**

Observing early stage rail axle bearing damage

N Symonds[1], I Corni[1,2], R J K Wood[1], A Wasenczuk[2], D Vincent[2]
[1] National Centre for Advanced tribology at Southampton, Faculty of Engineering and the Environment, University of Southampton, UK
[2] Perpetuum Ltd, Southampton, UK

Highlights

- On-board vibration sensors are correctly identifying failing rail axle bearings
- Bearings removed from trains with wear damage and full vibration history are being examined, and measured.
- The successful use of CT to identify and locate subsurface bearing damage has been shown.
- Premature rolling contact fatigue (RCF) of the stationary outer ring has been confirmed as the failure mechanism of the example presented.
- Large white etched layers have been observed

Observing early stage rail axle bearing damage

N Symonds[1], I Corni[1,2], R J K Wood[1], A Wasenczuk[2], D Vincent[2]
[1] National Centre for Advanced tribology at Southampton, Faculty of Engineering and the Environment, University of Southampton, UK
[2] Perpetuum Ltd, Southampton, UK

Abstract

A novel condition monitoring system has for the first time enabled reliable extraction from service and detailed forensic examination of failing rail axle bearings, before the usual catastrophic destruction of the evidence. Computed Tomography has been used to produce a map of the damage allowing targeted sectioning of subsurface cracking. Traditional metallographic techniques have revealed large white etched layers associated with the subsurface cracking, while observations with a scanning electron microscope have confirmed rolling contact fatigue crack propagation, possibly initiated from pre-existing electrical arcing damage of the raceways.

Keywords: Fatigue markings, Forensic engineering, Bearing failure, Railway engineering

1. Introduction

1.1. Axle bearing failures

Rail vehicle axle-bearing failure is a serious issue often resulting in service delays and potentially fire and derailment, with obvious risks to life. A 'dead' train on the railway line has implications for customer perception, operator and manufacturer reputation, along with large costs from penalties, recovery, train availability and repairs.

All bearings will eventually fail, if used for long enough. The 'old age' mechanism for most bearings is rolling contact fatigue (RCF), which can propagate from both surface- and subsurface-initiated failures. Subsurface microstructural changes due to RCF occur if the maximum Hertzian shear stresses exceed the elastic limit of the bearing steel. These changes may greatly reduce the fatigue life of bearings by initiating cracks, which lead to macro pitting on the bearing surfaces [Ref 1]. The cracks start at subsurface flaws within the material of the race and are driven by the repeated load from the passage of the rolling elements. These cracks spread and eventually rise to the race surface, releasing a 'spall' of material and leaving an RCF macro-pit. If allowed to continue, the running surface of the bearing becomes more worn and the passage of the rolling elements more disrupted [Ref 2]. Bearing failure due to material defects has been greatly reduced by using clean and properly heat-treated steels [Ref 3].

Bearing manufacturers provide life predictions; this information gives the operator a statistical indication (L_{10} or B_{10}) of when RCF might occur [Ref 4,5,6]. The operator then sets a service life (given in miles) and when a bearing has reached it, it must be replaced. This approach of giving a usage limit to bearings is common in safety critical applications (e.g. large bearings in helicopter gearboxes [Ref 2]. However, the life predictions are statistical and only as good as the loading data provided [Ref 3]. RCF life is significantly influenced by the material microstructure, which is inherently inhomogeneous, and therefore the RCF lives of a seemingly identical batch of bearings operating under identical load, speed, lubrication, and environmental conditions show a significant degree of scatter [Ref 1,5], so infantile failures can and do occur. However, premature failures of train wheel bearings have also been blamed by operators and design authorities on various operational issues including vibration, grease failure, overloading, misalignment, electrical shorts, wheel flats, installation problems and suspension design.

Figure 1 shows the condition of a bearing following catastrophic failure (one of two reported by Southeastern (LSER) over the 2012-2013 period. The outer ring has been removed; Figure 1a shows all that remains of the two inner (cone) rings, the central spacer, the 46 rollers and two molten polymer cages. Figure 1b shows a higher magnification view of the damage; it is interesting to note that the rollers have been smeared across the raceway and the shoulders of the inner (cone) rings have been worn down.

In addition to the serious catastrophic cases where the bearing has melted and fire is inevitable, many bearings are 'caught' in time either by experienced 'riders' listening for additional bogie noise or by passengers and on-

board train crew. LSER prematurely (before the service life expired) replaced 80 wheel-set axle bearings (i.e. 160 bearings) due to reported noise over a two year period (2011-2013).

1.2. Condition monitoring of bearings

Various technologies and approaches have been adopted to continuously monitor the state of bearings. For example, military helicopters have gearbox HUMS (Health and Usage Monitoring Systems) with additional wear debris monitoring and oil analysis. The former is a data recording of the temperature and vibration signature of the gearbox, which is downloaded and analysed at intervals. The latter is the chemical and physical analysis of the condition of the lubricants, looking for RCF debris [Ref 2]. These methods are not real-time but do give diagnostic warning of any changes in behaviour from 'normal'.

Hot axlebox detection (HABD) has been used in the UK national rail network for decades as a safety requirement. The HABD are sited either on-train for inboard or high-speed bearings, or trackside for outside axleboxes. Approximately 220 trackside HABD detectors are currently installed in the UK [Ref 7]. A bearing that is creating sufficient heat to trigger an HABD will already be in full failure mode. Therefore the train has to be stopped immediately causing disruptions to passengers and railway traffic. HABD detectors are expected to be phased out over the next 10-15 years leaving a requirement for a new diagnostic tool.

For train operators in the UK, two approaches to degradation diagnostics are currently available as 'state-of-the-art', (1) a trackside system e.g. Railway Bearing Acoustic Monitoring (RailBAM) by Siemens or Trackside Acoustic Dectection System (TADS) developed by TTCI in the USA both employing microphones to listen to passing wheel-set bearings [Ref 7] or (2) an on-board system by Perpetuum Ltd [Ref 8]. The latter approach (the subject of this paper) provides each wheel bearing with local real-time vibration monitoring using accelerometers. Neither method of detection (track-side or on-board) will prevent early bearing degradation, but similarly to the helicopter HUMS, each will alert the operators so early intervention (before HABD) is possible, preventing catastrophic outcomes and reducing maintenance costs.

LSER rail axle bearings used in this study are currently given a service life of 500k miles, which is 10% of the calculated L_{10s}, the basic rating life at 90% reliability expressed in operating mileage, as calculated using the basic method given in Ref 6. However, as described in Section 1.1, many bearings do not survive to this (500k miles) milestone, suggesting that the in-service environment (on which predicted lifting is based) is not fully characterized and understood by the rail and bearing industries. LSER have now fitted the Perpetuum Ltd on-board condition monitoring system to 148 trains. Each train (unit) comprises of 3 to 5 passenger cars; each car has a bogie at either end containing two wheel-sets (i.e. 4 wheels). Therefore the typical train has 32 axle bearings. The system provides one sensor per wheel; LSER have nearly 5,000 wheels being monitored. The system highlights when a sensor detects an increasing vibration signature, isolates it as a bearing or wheel issue and reports it in real-time to the train operator. The bearing/wheel can then be removed/maintained at the depot at the next maintenance cycle.

Using the on board condition monitoring sensor an operator can look only for changes in vibration/temperature. The absolute values, although measured, are lacking in meaning and any thresholds of the system are arbitrary. Similarly a trackside system has the same limitations. The ultimate deliverable of this project, which will have a direct and immediate impact to the industry, is to produce a feedback loop of knowledge where an accurate assessment of bearing damage and remaining life can be correlated to in-service measured parameters of bearing vibration. This will provide the ability to set meaningful thresholds to axle monitoring. Using a dependable diagnostic system, operators could:

- Safely increase service intervals, increasing asset availability and reducing through-life costs.
- Prevent 'dead' trains blocking the line due to unexpected bearing failures (and possibly fires).
- Improve asset availability
- Reduce bearing replacement costs (from £100,000s to £100s) by removing the risk of penalty costs from blocking the line and 'dead' train recovery costs.

In addition to identifying damaged wheels and bearings the captured on-board vibration data is an accurate record of the in-service vibration environment to which the local components (including the bearing) are subjected. This will provide data for accelerated testing and modelling solutions, which in the longer term could lead to new bearing designs tailored to produce a longer life expectancy.

1.3. Aims of this paper

The novel approach of this work is the access to real *ex-situ* (as opposed to laboratory-generated) examples of early stage failures of bearings (thanks to a collaboration with LSER and Bombardier) combined with the in-service vibration history of the bearing (thanks to the collaboration with Perpetuum Ltd). The overall objectives of this project are:

- To identify the in-service bearing failure mechanisms by applying forensic engineering inspection techniques to damaged bearings.
- To demonstrate the ability of the Perpetuum vibration sensor to identify failing bearings at a suitably early stage.
- To link the damage location (rollers, rings, cage) to the vibration signature to help predicting the remaining bearing life and thereby give confidence to the operators to safely increase service intervals.

This paper was written to introduce the reader, and the delegates of the ICEFA VI, to our on-going work and to present some initial results. This paper also highlights the approach and the techniques employed to examine the removed rail axle bearings. These methodologies may benefit other researchers conducting physical examinations of monitored bearing/gears in other comparable industries such as aerospace or power generation.

2. System details

2.1. The sensor

Figure 2 shows a wireless sensor node (WSN) bolted to a wheel bearing housing. It is important to note that the sensor is sited on the inboard side of the housing and on the outboard side of the wheel. Each WSN acts independently to the other 31 (assuming a 4 car train), turning on, recording data and wirelessly returning key parameters to a central unit on board of the train. This unit forwards the data to an Internet Cloud Database. The WSNs are self-powered by vibration harvesting. This emerging technique has been made possible by the decreasing power budget of sensor and wireless technologies.

The sensor at the heart of the WSN is a tri-axial accelerometer that records 16,000 points per second per axis, aligned to record the X (vertical), Y (horizontal) and Z (direction of the axle) accelerations present in the system. Full details of the parameters recorded by the WSN are given in [Ref 9]. The WSN collects 192,000 data points over a 4 second recording window, irrespective of train speed. This raw data is used locally to calculate the peak and root mean squared (rms) values of each axis. These data along with the train number, wheel position, date and time, speed of the train, GPS location, direction of travel and local temperature are all transmitted. Three minutes later the process is repeated. Depending on the train mileage, on average 300-400 data parameters are received from each WSN daily.

2.2. The bearings and their environment

There is not a standard wheel and bearing configuration in use in the UK. The bearings available for this study came from Bombardier vehicles operated by LSER. Figure 3a shows an in-service train wheel, with the bearing housing outboard respect to the wheel and positioned under the suspension. Figure 3b shows one end of a wheelset without the bearing, the axle shaft for the bearing fitment is on the outboard side of the wheel.

The bearings analysed in the current work are termed Compact Tapered Roller Bearing Units (CTBUs) by their manufacturer SKF, see Figure 4 [Ref 10]. Each CTBU (Figure 5a) consists of:

- An outer ring with an exterior diameter of 210 mm with two symmetrical cup races (Figure 4 (27));
- Two inner rings (cones) (Figure 5b) with 40 mm wide tapered surfaces (races), upon each of which rotate 23 tapered rollers.
- The rollers are kept into place by a polymeric cage (Figure 5c).

The inner rings are fitted directly onto the protruding axle shaft (Figure 3b) and are separated by an 11 mm wide central spacer (Figure 5c and 4). Inboard of the bearing on the axle shaft is a backing ring (Figure 4) separating the bearing from the wheel hub. The lubricant has been reported as SHELL Alvania 2760B.

The specifications of the materials have not been provided to the authors, however metallographic examinations involving micro-Vickers hardness testing and destructive spectrographic analysis (carried out by Southdown Materials Testing Limited) (Tables 1 and 2) revealed that the outer ring, inner ring and rollers were all through hardened and made of 1C -1.5Cr steel type alloy [Ref 11] consistent with SAE 52100 [Ref 12]. It was interesting to note that the outer ring was the softer component and the rollers were the hardest (Table 2) by 2 HRC points, a condition which has been linked to improved rolling contact fatigue life in 534A99 (1C-1.5Cr type) steels (equivalent to 100Cr6 steel to BS EN ISO 683-17) [Ref 13].

Table 1: Chemical composition measured by destructive spectrographic analysis of the bearing components compared to 1C-1.5Cr steel [Ref 11].

Element %	Inner rings	Rollers	Outer ring	1C-1.5Cr
Carbon	1.07	1	1.08	0.98-1.10
Silicon	0.29	0.25	0.3	0.15-0.35
Manganese	0.38	0.26	0.31	0.25-0.45
Phosphorus	0.009	0.017	0.006	0.025 max
Sulphur	<0.005	0.011	<0.005	0.025 max
Chromium	1.53	1.34	1.52	1.30-1.60
Nickel	0.11	0.17	0.12	0.25 max
Molybdenum	0.04	0.06	0.06	0.10 max
Copper	0.17	0.18	0.19	
Titanium	0.01	0.01	0.01	
Aluminium	0.039	0.046	0.031	
Cobalt	0.01	0.016	0.013	
Tin	0.007	0.008	0.011	

Table 2: Average of through hardness values of bearing components as measured by micro-hardness tester, original values in HV0.2, converted to HRC.

Hardness	Inner rings	Rollers	Outer ring
Micro-Vickers HV0.2	812	841	753
HRC	62	64	60

It can be shown from the GPS data recorded by the WSN that the trains travel at speeds up to 100 mph (44 $m \cdot s^{-1}$), the wheel diameters range from 840 to 780 mm. Therefore the axle bearings are operating up to 1000 rpm. Based on a bore of 130 mm the speed factor dN which is the product of the bearing bore (d mm) multiplied by the max speed (N rpm) can be calculated as 140k $mm \cdot min^{-1}$. High-speed bearings are considered to have dN values of 10^6 [Ref 3], therefore rail axle bearings operate in the low-speed, high load regime. The inner rings rib diameter is 156 mm. The rib speed can be calculated to be up to 8.2 $m \cdot s^{-1}$; it is well known that in this regime grease lubrication should be adequate to avoid problems [Ref 14].

Data provided by LSER regarding vehicle masses have been used to determine upper working static loads on each CBTU. Assuming max passenger loading (100 passengers at 75 kg including luggage each) then the carriage mass could be 47.4 – 52.8 tonnes. Following the method detailed in [Ref 6] the bearing load (per bearing) can be calculated to be ≈ 70 kN, i.e. 35 kN per race if evenly loaded across the two races. Railway Group Standard [Ref 15] states that (bearing) designs must withstand the inertial forces associated with a proof load of 75 g_0 (units of standard gravity, g_0) and 10,000,000 cycles of 25 g_0. For example, if the axle is

accelerated at 75 g_0 and the axlebox weighs 100 kg, the axlebox reacts against the axle (through the bearing) with an inertial force of about 75 kN; this is on top of the existing loads due to the mass of the carriage.

3. Techniques and methods for investigating the damage

The large number of monitored bearings (nearly 5,000) running on LSER trains has provided this research project with access to several bearings to examine. The techniques and approaches adopted to examine the bearings need to fulfil several requirements:

- produce quantifiable values describing the level of damage to each bearing;
- provide opportunities to observe the damage mechanisms;
- allow in-depth analysis of possible causes or influencing factors;
- repeatability;
- take place in a systematic order (i.e. non-destructive first).

The stages adopted are shown in a flow diagram (see Figure 6); some techniques (all listed on the right of the figure) are a 'standard' requirement and some are for specific follow-up investigations. For example, Alicona, micro-CT (Computed Tomography), SEM (scanning electron microscopy) and EBSD (Electron Backscatter Diffraction) were considered techniques to be used as necessary, whereas the Talyrond analysis and macro CT-scanning were carried out for each bearing.

Profilometry of the outer ring races was performed using a Talyrond 595 instrument based at Taylor Hobson Limited (Leicester, UK). Following the collection of the profilometry data the bearings were 'cropped' into manageable arcs (Figure 7) using a water jet cutter (Safire, UK). Prior to cutting, black wax W (Apiezon Products M&I Materials Ltd) was applied to the area of interest to protect it from any degradation. Due to the tendency of the bearing material to corrode quickly, WD40 was liberally applied and the sections stored in low humidity containers.

The arc shape provided access for several techniques:

- A Stemi 2000c Zeiss macroscope with oblique lighting and DSLR camera was used to examine and record regions of interest.
- An Alicona InfiniteFocus 3D optical non-contact profilometer was used to record the form and surface roughness of identified regions.
- A Nikon/Metris 'hutch' 450 kVp microfocus system, based at the University of Southampton was employed to CT the outer ring arc, using a curved linear detector array with setting of 420 kV at 143 µA, 6 mm of copper filtration, producing 200 ms exposure per line, with 1801 projections (lines) per sinogram (slice).

Following the application of the above techniques the outer ring arc (and corresponding inner ring and rollers) were sectioned to isolate areas of interest for further examinations. Cutting was carried out using a diamond blade on a Metcatome T210 with pulse setting (1500 ms on and 1000 ms off), disc speed of 3200 rpm and a feed rate of 0.3 $mm \cdot s^{-1}$. PolyFast, a Struers thermosetting product (conductive bakelite resin with a carbon filler), was selected to hot embed the bearing samples. A Simplimet 2000 with 6 min heating to 180°C and a pressure of 250 bar and 4 min cooling time was used to create 30 mm diameter 'micros'.

The micros were then ground and polished on an ATA Saphir 520 automatic machine using the cloths and settings listed in Table 3. Care was taken to immediately clean and dry the samples as the freshly polished bearing surfaces quickly showed signs of corrosion if left exposed to moisture for more than several seconds. The resultant polished micros were either viewed as polished or etched to reveal microstructure. The four etchants used are listed in Table 4.

The micros were examined firstly using an Olympus BX51 microscope and subsequently with a JEOL JSM-6500F scanning electron microscope (SEM). The SEM was also used to examine sections of the bearing fracture surface and debris, which did not form micros – i.e. plan view not cross-section.

Table 3: Grinding and polishing steps applied to the micros. The micros were rinsed in distilled water and methanol and dried between steps.

Cloth	Solvent	Force	Rpm	Time

MD Piano 120	Water	30 N	300	Until flat
MD Allegro	Dia Pro Allegro-Largo 9 µm	30 N	150	4 min
MD Dur	DP Dur 1 µm	30 N	150	4 min
MD Chem	OPS or OPU	15 N	150	1 min

Table 4: List of etchants used for the examination of the polished samples.

Etchant	Composition
Nital	1 to 4% HNO_3 (conc) Methanol
Picral	1 to 4% picric acid (contain 35% water) (from Aldrich) Ethanol
Klemm's 1 reagent (Reference [Ref 16]	1% $K_2S_2O_5$ (from Sigma Aldrich) saturated solution of $Na_2S_2O_3$ in water
Nital + Picral	2% HNO_3 (conc) 2% picric acid (contain 35% water) (from Aldrich) Ethanol

4. Results

4.1 Introduction

The initial results of the forensic engineering examination of one damaged CTBU (Figure 5) are described. This CBTU was identified by the on-board condition monitoring system as displaying higher vibrations than others bearings from the same side of the train (Figure 8) (as described in [Ref 9]). The outer ring of the bearing is shown in Figures 7 and 9. The results below are used to demonstrate the techniques adopted in this work.

4.2 Vibration data

The vibration data recorded by the WSNs provide an insight into the on-board train environment; even without any faulty bearings or wheels there are sources of vibration in the system (see Figure 8a). The effects of speed and other sources of vibration have been explored and are reported in [Ref 9]. The rms X data in Figure 8a show in-service acceleration values up to 2 g_0; however peak values of up to 20 g_0 have been regularly recorded. This local vertical acceleration upon the bearing will magnify the bearing load.

When a bearing becomes damaged the measured vibrations increase, see Figures 8b-c (yellow to orange to red data points). In the example shown in Figure 8 the increase in vibration took place over three months prior to replacement. Once the bearing was replaced the vibration levels dropped (green data points) back to within the normal 'background' vibration level (Figure 8d). The bearing had completed 4 years 9 months of service and accumulated 557,397 miles at replacement.

Further statistical studies can be performed on the vibration data to determine the change in variance, mean and peak rms X values. The changes in these values over the last 18k miles prior to replacement are shown in Figure 10. Note 'pre' and 'post' have been used to identify the vehicle mileage relative to the bearing replacement.

4.3 Optical examinations

When the suspect bearing was removed and disassembled at the train depot, significant damage to the rolling surface of the inboard side race of the outer ring was found. Figure 9 shows an image of the failed outer ring in 'as-received' conditions.

Visual examinations revealed 95 mm of damage which equated to 60° of wear, see Figure 7. The damage was centralized with no obvious signs of misalignment. Misalignment can be an issue for single row tapered roller bearings [Ref 4]; whereas double row bearings are less likely to suffer from misalignment problems.

Within the outer ring damage, two line features were observed, marked A and B in Figure 7. The line features were aligned with the direction of rolling and located toward the centre of the outer ring, i.e. where the thin end of the tapered rollers would pass. As marked on Figure 7 the line features were located 9 mm and 17 mm away

from the edge of the race. Line feature A appeared to be present for 90% of the damage length while feature B was shorted but wider (Figure 7).

A closer inspection revealed that the line features were deeper than the surrounding material (see Figures 11 and 12). The direction of propagation of several fatigue cracks have been marked with dashed arrows in Figures 11 and 12, the origins of these fractures appear to be the line features. Furthermore, it was noted that the line feature B appeared to have a very smooth (surface roughness Ra of only 1.2 μm was recorded using Alicona Infinite Focus), yet rippled surface, when compared to the rest of the damaged raceway, see Figure 12.

Upon receipt of the failed CTBU, access was gained to the inner rings by cutting through the cage and releasing the 23 tapered rollers, a note was made to their order around the ring. Figure 5b displays both inner rings. All the rollers from the inboard (failed) side were examined revealing debris denting on all of them. Moreover, three consecutive rollers showed additional indications of electrical pitting damage, see Figure 13. Examination of the inboard inner race revealed the same discrete groups of pitting marks, these marks exactly matched the location and distribution noted on the rollers, see Figure 14. Closer examination of the roller pitting marks revealed evidence of the local heating effects typical of electrical damage, see Figure 15.

A 3 cm wide central strip of the sample (see Figure 16) was measured using Alicona. A line profile was created from the strip of data recorded and used to determine the depth of the line features A and B positioned 400 and 600 μm below the original race surface.

4.4 CT examination

Computed tomography (CT) was used to determine non-destructively the condition of the bearing below the worn raceway and also to provide data to calculate the volume of material loss. 110 slices were taken across the sample shown in Figure 7; although it was possible to produce a higher resolution, a step interval of 1 mm was chosen. Prior to scanning, notches were cut into the side of the arc section (Figure 7), the slices stacked together created the rendering shown in Figure 17, in which the three locating notches are visible in slices 31, 58 and 79. By putting physical marks in the bearing prior to scanning, the location of identified features can be readily translated from the virtual to the actual curved tapered surface.

Due to the thickness and density of the steel the resolution of each image slice was 0.0523 mm per pixel; this was deemed sufficient to identify subsurface cracking. Subsurface cracking was noted at slices 19 to 21 (slice 19 is shown in Figure 18a); a larger curved crack was observed in slices 48 to 59 (slice 53 is shown in Figure 18b) and again between slices 67 and 86 in the same position of the raceway but with a bisecting secondary crack (slice 77 is shown in Figure 18c). The locations of the line features A and B are marked upon the CT images, it was noted that subsurface cracking was coincident to line feature A (Figures 18b-c).

4.5 Volume loss

Five line-traces were made with surface profilometry along the damage, in the rolling direction, at distances 5, 10, 20, 30 and 35 mm from the inboard side of the 40 mm track. Figure 19 shows the 10, 20, and 30 mm traces; the profiles have been fitted to the radii of the track creating the line profiles shown. For clarity the y-axis data from the 10 mm and 20 mm traces have been offset by +2 mm and +1 mm, respectively. It can be seen from Figure 19 that a significant depth of material has been lost; the maximum documented depth (0.824 mm) was recorded at the 30 mm position. Interestingly the minimal wear was observed down the centre of the bearing track at the 20 mm position. The areas of worn material measured were: 27 mm^2 at 5 mm, 36 mm^2 at 10 mm, 22 mm^2 at 20 mm, 29 mm^2 at 30 mm, and 32 mm^2 at 35 mm. This gives an average wear loss of 29 mm^2. This value can be multiplied for the 40 mm width of the track to obtain an approximate volume loss of: 29 x 40 = 1,162 mm^3. This value was then compared to the volume loss calculated using the CT scanning data.

Using software 'Fiji' each CT slice was converted to a black and white image; the missing area of each slice was measured. Plotting these values, see Figure 20, produces a chart with a form similar to the profilometry data (Figure 19 – 30 mm), and can be thought of as an average or smoothed profile measurement. The total volume missing was calculated from the CT data to be 1,245 mm^3 or 1.2 cm^3. Comparing the two methods of calculating volume loss revealed that there was a 7% difference. Interestingly, the chart shown in Figure 20, appeared to show a cyclic pattern.

The Alicona offers a third method to measure volume loss, via multiple digital imaging under microscope lenses. The three-dimensional profilometry results would then be curve fitted to the original tapered bearing track surface to calculate the volume missing. Unfortunately, it was found that the geometry of the part (Figure 7) did

not fit under the instrument. Smaller wear scars could be measured in one session and therefore this method has been successfully used to examine other failed CTBU's [Ref 9], hence its inclusion in the method diagram Figure 6.

4.6 Metallography

Initial examinations were performed upon bulk material samples, away from the damaged surfaces, to view the microstructure characteristic of the bearing steel. Figure 21 provides an optical microscope image showing the microstructure of the inner ring, the same microstructure was observed for the outer ring and the roller samples examined. In Figure 21, it is possible to discern the evenly distributed very fine carbides typical of the 1C-1.5Cr alloy [Ref 17,4]. The 52100 steels are quenched and tempered before usage and their material properties are significantly influenced by the characteristics of the carbides [Ref 17]. Studies have indicated that the uniform dispersion and the fineness of carbides (M7C3/M23C6) are ideal for improved mechanical properties and that bearing endurance can be further improved by carbonitriding [Ref 17]. Micro-hardness testing performed on cross-sections of the bearing elements found no distinction between the surface and bulk hardness properties, indicating that these axle bearings had no surface treatments.

Micro-sections were taken through a suspected site of electrical pitting (highlighted on the right-hand roller shown in Figure 13). Etchings with Nital (Table 4) revealed evidence of microstructural changes consistent with local heating, confirming that the isolated sites of damage were due to electrical arcing, see Figure 22.

Micro-sections were taken through the damaged outer ring at locations highlighted by the CT work, see Figure 18. Stitching together optical microscope images taken using a x5 optical lens, it is possible to resolve the full width of features and their position relative to each other (see Figure 23). Figure 23a is a section taken in the region of slice 53 (see Figure 17), the corresponding CT image of the whole slice can be seen in Figure 18b. Highlighted in Figure 23a is the subsurface crack, previously identified and two regions of material that were revealed as white after etching. The two white layers correspond to the locations of the two line features labelled A and B in Figures 7 and 12. Figure 23b is a section taken in the region of slice 77 (see Figure 17), the corresponding CT image of which is shown in Figure 18c.

The same white layer (line A) found in slice 53 was also found in slice 77 (see Figure 23c), 24 mm away. The white layer (line feature A) was measured to be approximately 2 mm wide, up to 48 µm deep (see Figure 24) and orientated at about 45 degrees to the bearing surface. The second white layer shown in Figure 23a(labelled as line feature B) was measured to be 1.2 mm wide and up to 38 µm deep (Figure 25). Micro-sections were taken outside the 95 mm of damaged raceway; no evidence of the white layer was found.

Higher magnification views of the white layers (Figures 24 and 25) revealed that they were associated with subsurface cracks or fracture faces in the bulk material. Moreover, the microstructure of the white layer was significantly different from that of the bulk material, this was especially evident when the micro was analysed with an SEM in secondary electron mode, see Figure 26. The upper portion of Figure 26 shows the white layer, while the lower portion shows the expected lath structure of retained martensite and the globular cementite of the bulk bearing material. Figure 27 provides a view of the white layer and bulk material in back scatter mode.

The higher resolution and magnification offered by the SEM (over optical microscopy) was used to examine the wear debris and isolated areas of the bearing damage. Debris, previously extracted from around the polymeric cage and the rollers of the inner ring, were filtered, cleaned and examined. Figure 28 shows examples of the characteristic 'petal' shape of the debris, commonly associated with rolling contact fatigue [Ref 3]. There are four typical types of wear particles that have been recognized as being representative of rolling contact fatigue: microspall (or micropit) particles, laminar particles, chunky particles and spherical particles [Ref 17]. Based on the size, aspect ratio and surface features the debris flakes shown in Figure 28 are consistent with over-rolled laminar particles.

Further evidence of a fatigue propagated fracture surface was observed on the damaged rolling surface of the bearing. Figure 29a provides a montage of SEM micrographs showing a large section of bearing raceway that would have broken free if the bearing had not been removed from service. Evidence in support of this can be found in the CT image slice 19 (Figure 18a) that clearly displays subsurface cracking. Higher magnification of the fracture surface (Figure 29b) revealed step features, consistent with a cyclic (fatigue) propagation mechanism.

5. Discussion

The implications for the operator and passengers of a catastrophic rail axle bearing failure have been introduced; the photographic images of Figure 1 display the resulting bearing conditions. It can be assumed that during this failure the grease broke down and subsequently the bearing (through frictional heating) became hot enough to cause melting of the cage. The rollers were either expelled or smeared across the races. In this particular case, there was also a local fire in which the rubber suspension system (located above the bearing housing (see Figure 3a)) burnt; fortunately the wheelset remained on the track. It is almost impossible to determine after the event what initiated the bearing failure as the bearing condition is so degraded. The trackside HABD system has a small window of opportunity to catch a bearing that has become hot enough to be detected, but still has not yet caught fire. This limitation among others has led to the decision to phase out HABD systems in favour of acoustic and vibration monitoring approaches that offer the opportunity to identify bearing failure at an earlier stage. A significant benefit of the earlier detection and removal of failing bearings is the opportunity to examine the damage prior to catastrophic failure and melting.

There is a requirement to link vibration (or acoustic) signatures to levels of physical damage; only then will any monitoring system be able to provide true quantitative diagnostics. The first step towards this goal is to examine ex-situ rail axle bearings for which complete vibration histories have been recorded. As highlighted in Section 3, a systematic approach for the examination of the failed bearings has been adopted here. This approach has been optimised to provide both qualitative and quantitative data regarding the condition of the failed bearings. Specific tools that have been successfully utilized are: profilometry and macro-computed tomography (CT). The former has been used to define the shape and form of the damage, the latter to provide a map of the subsurface damage to aid later destructive examinations.

The initial examination of a removed rail axle bearing, that displayed both an increasing vibration signature (Figure 8) and significant outer ring damage (Figure 9), has been presented. This example bearing (and others like it [Ref 9] confirms that the monitoring system currently fitted to LSER trains is correctly identifying failing bearings, and is doing so prior to catastrophic melting and destruction of the bearing.

This particular bearing was allowed to run past the 500,000 mile operators' service limit because it was being monitored by the Perpetuum sensor. It is interesting to note that the calculated L_{10s}, is 5,000,000 miles, suggesting that 90% of all the bearings should achieve this life. With the sensor in place there is the potential for the operator to confidently raise the service life limit, thereby increasing time between services and reducing costs.

As shown in Figure 8 the vibration signature from the WSN decreased to 'background' levels when the bearing was replaced. If the wheel was characterised by wheel flat damage (a suspected cause of subsequent bearing failure) or RCF the vibration values would have remained high after the bearing was removed. However, it is not known if there had been a previous wheel flat or RCF of the wheel during the life of the bearing; such an event would have reduced the bearing life by opening up any existing subsurface cracks present (however small). Events that cause shock loading to the system will reduce the RCF life of the bearing; for a semi-quantitative approach one could apply Miner's rule. Wheel defects that are known to produce shock loadings can be caused by (i) wheel slip during braking, or (ii) wheel spalling due to advanced RCF. Additionally, Perpetuum Ltd have extrapolated from their measured WSN data that the maximum lifetime loads are in the order of 200-400 g_0, or 200-400 kN for a 100 kg axlebox. This paints a significantly harsher environment than that described by the Railway Group Standard [Ref 19], and could be the ultimate cause of the RCF of the outer ring.

A statistical inspection of the vibration data recorded within the last 18k miles before bearing removal was made, see Figure 10. It can be seen that the sample variance, mean and max values of the data were all greater than the reference values taken several thousand miles later with the newly fitted bearing. The mean values of the rms X data show a monotonic increase in value, which reached 2.34 g_0 over the last 3k miles of use. [Ref 9] made a tentative link between mean value of rms X at removal and the size of the damage found. However, the bearing removed in the current case had significantly more wear (1,245 mm^3 versus 900 mm^3) yet lower mean rms X value (2.34 g_o versus +3 g_o) at removal than those given. This indicates an additional level of complexity, for example there is a possible smoothing effect to the vibrations with time due to the repeated passage of the rollers over the damaged area.

Two separate subsurface layers (distinct from the bulk material) were identified. Observed from the surface they appeared as two line features (labelled A and B) running in the rolling direction of the bearing, see Figure

7, 11 and 12. When sectioned, polished and etched, the layers retained a white hue when viewed with optical microscopy. The composition of the white etched layers found in the sample has not yet been determined. It can be assumed that they are not inclusions, as EDAX examination did not find any unusual compositional elements present. In Figure 27 the white etched layer can be differentiated based on contrast; elements of greater atomic mass (the white layer in this case) appear brighter in a back-scattered electron image. It is postulated that the layers are transformed bulk material, which occurred due to large subsurface shear stresses. Further inspection and examination of the white layers with nano-hardness and EBSD is planned and will be reported at a later date. Whatever their composition, the white etched layers clearly contain many micro-cracks and voids (see Figures 24-27) and are present across most of the damaged arc (Figure 7). The layers are also externally smooth with clearly defined edges and as such represent a significant stress discontinuity with the surrounding bulk material (no local 'keying' or blending). The layers have been identified as the origin sites of fractures (see Figures 11, 12, 23 and 24). Those fractures display features consistent with a cyclic crack propagation mechanism, confirming the presence of RCF. RCF was further identified through the shape and form of the debris collected from the bearing grease.

The maximum and average depth of damage to this current bearing were 0.824 mm and 0.215 mm, respectively; the damage covered the full width of the raceway and extended to 60° of the circumference. This large width to depth ratio is typical of RCF bearing failures, which are driven by the Hertzian shear stresses. Equations reproduced in [Ref 2] can be used to determine the depth of maximum Hertzian shear stress for a line contact of a roller on a flat surface. Approximating the bearing taper geometry and using a static bearing loading of 35 kN, the Hertzian depth can be found to be ≈ 0.58 mm, however this depth increases with loading. Interestingly the white etched layers (see Figure 16) were found at depths of ≈ 0.4 mm and 0.6 mm (A and B respectively), which are clearly within the band of maximum shear stress. This result suggests that the high loading event created the two layers.

The causes of premature RCF of bearings can be split into two groups: (i) the influence of environment and set-up (e.g. application of a heavier external load than anticipated, preloading on account of incorrect fits or excessive drive-up on a tapered seat, oval distortion owing to shaft or housing seat out-of-roundness, axial compression, for instance as a result of thermal expansion.), or (ii) the result of other types of damage (e.g. indentations, deep-seated rust, electric current damage or smearing). There was no evidence to suggest that a unusual pre-load, distortion, or thermal effects had influenced the bearing examined. However, the bearing did display electrical current damage on the inboard inner ring and on three consecutive rollers from the same side. No evidence of electrical damage was seen on the outboard half of the bearing, but electrical pitting was observed on the matching bearing at the other end of the wheel-set.

All sites of electrical damage observed were 'minor', i.e. they were at discrete locations and did not surround the rollers or inner ring and only affected three rollers. The path for the electrical arcing would have passed through the outer ring, and would have created similar localized damage. The question remains: did the electrical event influence the RCF of the outer ring? It is not known when in the life (4 years and 9 months) of the bearing the electrical damage occurred. The lack of subsequent (RCF) damage to the rollers and inner ring, or to the other bearing from the same wheel-set, suggest it was a recent event, and therefore would have had not played a part in the outer ring failure. However, if the electrical event did precede the RCF, the electrical damage to the outer ring raceway combined with a heavier external loading (suggested by the recorded loads and the presence of the white etched layers) could have caused the resultant outer ring bearing failure. Equally, if the external loading was large enough, or there were regular shock loading events, RCF would have occurred even without any electrical damage.

6. Conclusions

- On-board vibration sensors are correctly identifying failing bearings, at a stage early enough for the train to go into a planned maintenance cycle.

- Bearings removed from trains with wear damage and full vibration history are being examined, and measured, with the ultimate aim of linking vibration to damage.

- The successful use of CT to identify and locate subsurface bearing damage has been shown.

- The examination of a bearing has been presented. Premature rolling contact fatigue (RCF) of the stationary outer ring has been confirmed as the failure mechanism. Evidence of electrical damage and high subsurface shear loads has been presented as possible initiating and driving effects.

7. On-going/Future work

- Further real-life bearing examples removed from trains will be examined for evidence of pattern behaviour.

- Further examination into the influence of electrical damage on rail axle bearing damage will be investigated.

- The white etched layers observed during the examination of the presented bearing will be further identified and characterized using EBSD and nano-hardness testing.

8. Acknowledgements

The authors gratefully acknowledge the EPSRC IAA support for funding, Dr Liam Goodes (nCATS, University of Southampton), Mr Sam Hopkins (Ametek) and Mr Gavin Fuller (Southeastern) for their assistance during the work. Thanks are also given for the funding support given by Perpetuum Ltd.

References

1. Sadeghi F, Jalalahmadi B, Slack TS, Raje N, Arakere NK, A review of rolling contact fatigue. Journal of Tribology, V131 Iss4 2009 pp041403(1-15)
2. Symonds N, Condition monitoring and failure analysis: powerful tools for modern military helicopters. Insight - Non-Destructive Testing and Condition Monitoring, published by The British Institute of Non-Destructive Testing, Volume 47, Number 8, 1 August 2005, pp. 472-477(6)
3. Savaskan T, On the wear and failure of high speed roller bearings. Wear, 116 (1987) pp.361-380.
4. Gurumoorthy K, Ghosh A. Failure investigation of a taper roller bearing: A case study. Case Studies in Engineering Failure Analysis. Vol1, Iss 2, April 2013, pp. 110-114
5. Vlcek BL and Zaretsky E, Rolling-element fatigue testing and data analysis – A tutorial. Tribology Transactions Vol54, Iss4, pp. 523-541, 2011.
6. SKF: Bearing calculation. Extract from the Railway technical handbook, volume 1, chapter 5, page 106 to 121
7. Marsh S, Sound Investment. The Rail Engineer Jan 2013, Iss 99, p. 47-50
8. Owen R, No bearing on acoustics? Think again. Institute of Acoustics: Acoustics Bulletin July/August 2014 pp35-37
9. Corni I, Symonds N, Wood RJK, Wasenczuk A, Vincent D, Real-time on-board condition monitoring of train axle bearings, manuscript in preparation, IMECHE: The Stephenson Conference, April 2015.
10. SKF: Bearing designs, tapered roller bearing units. Extract from the Railway technical handbook, volume 1, chapter 4, page 76 to 87.
11. Hollox GE, Hobbs RA, and Hampshire JM. Lower bainite bearings for adverse environments. Wear, 68:229-240, 1981.
12. Bhadeshia HKDH Steels for bearings, Progress in Materials Science. Vol 57 Iss 2 Feb 2012, pp 268-435.
13. Neale M J, "The Tribology Handbook" Second Edition 1995 ISBN 0 7506 1198 7
14. The Timken Company "Timken Bearing Damage Analysis with Lubrication Reference Guide" 2.5m 06-11: 29 order No. 5892, 2011. http://www.timken.co.uk/EN-US/Knowledge/ForMaintenanceProfessionals/Documents/Bearing-Damage-Analysis-Reference-Guide.pdf accessed 4 September 2014.
15. Railway Group Standard GM/RT2100 Iss5 2012, published by RSSB.
16. Vander Voort GF, Color Metallography, ASM Handbook, Volume 9: Metallography and Microstructures, p 493–512
17. Rajan K, Joshi V, Ghosh A effect of carbonitriding on endurance life of ball bearing produced from SAE 52100 bearing steels. Journal of Surface Engineered Materials and Advanced Technology, 2013, 3, pp. 172-177

18. Ding J, Determining fatigue wear using wear particle analysis tools. Practicing Oil Analysis, September 2003
19. Railway Group Standard GM/RT2100 Iss5 2012, published by RSSB

Figure list

Figure 1 90mm 500dpi

Click here to download high resolution image

(a)

(b)

Figure 2 90mm 500dpi
Click here to download high resolution image

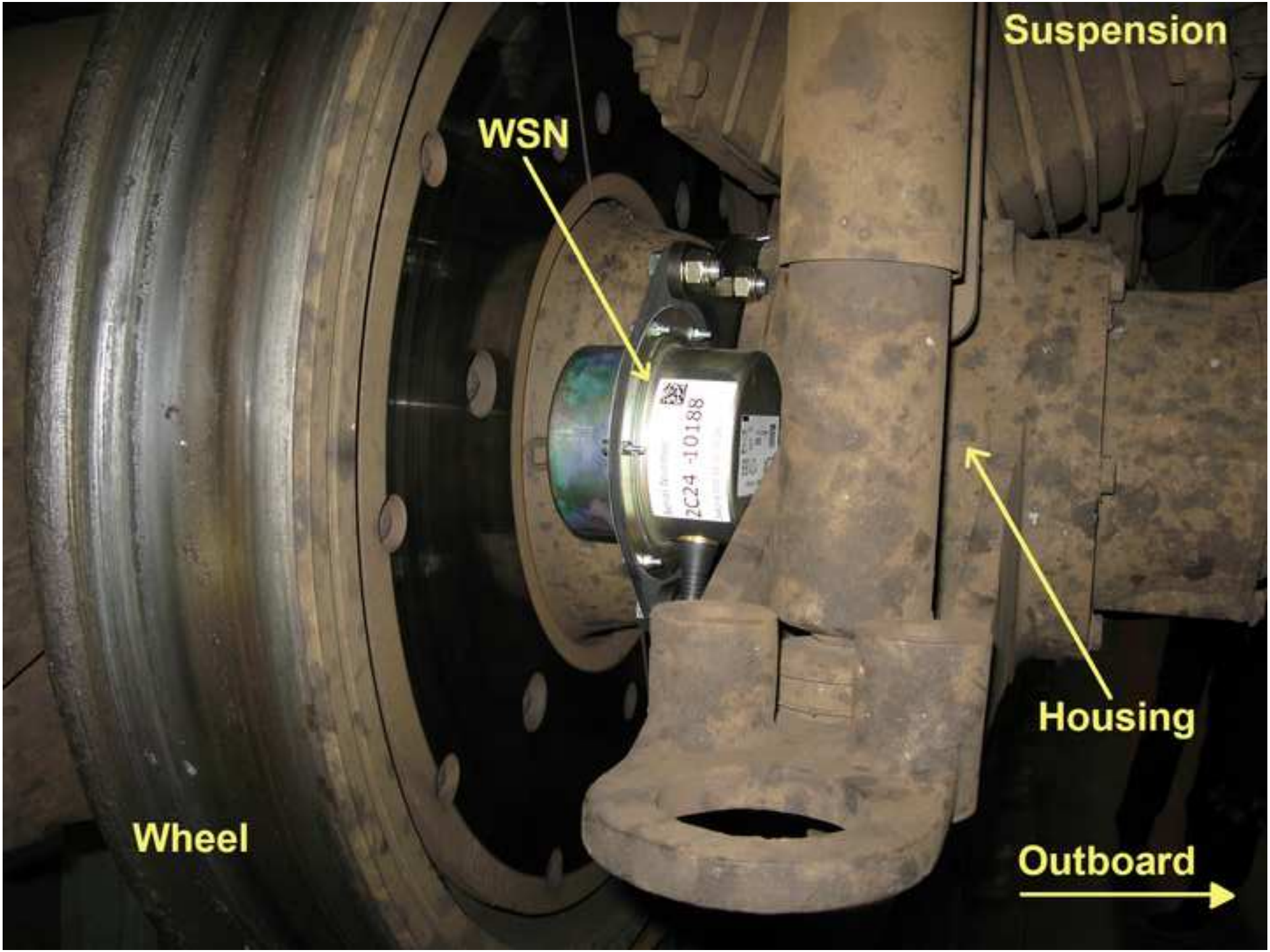

Figure 3 90mm 500dpi
Click here to download high resolution image

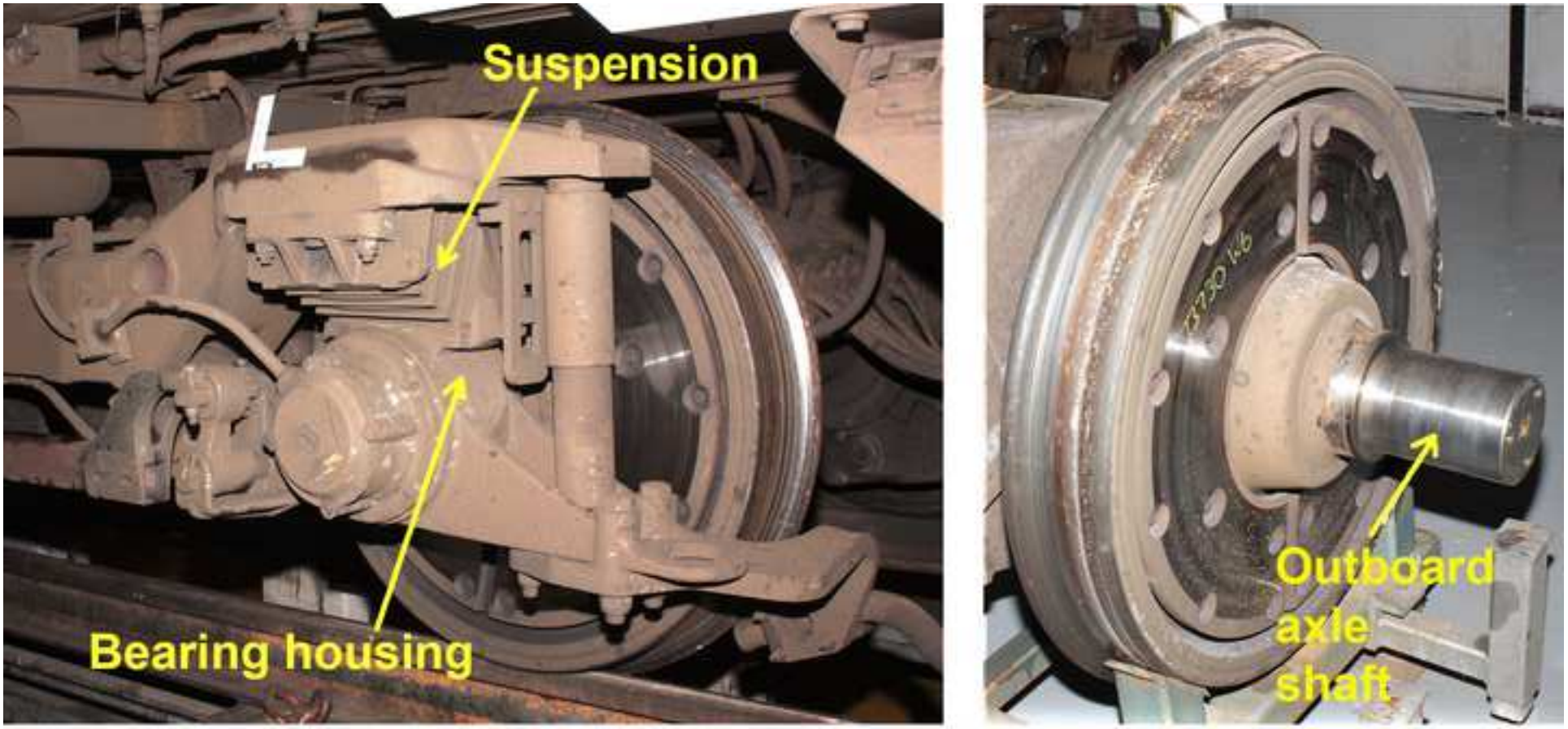

(a) (b)

Figure 4 90mm 500dpi
Click here to download high resolution image

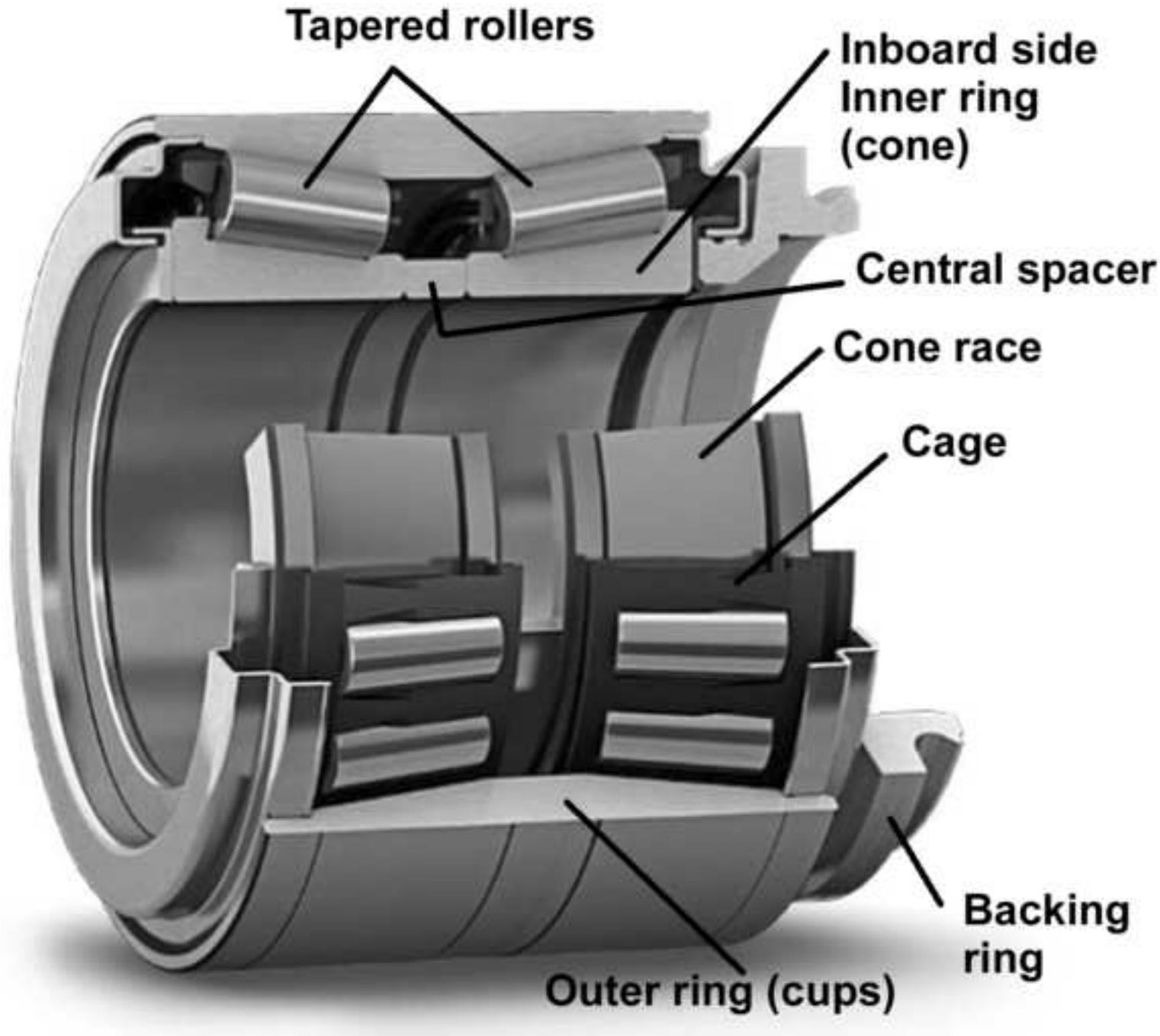

Figure 5 140mm 500dpi
Click here to download high resolution image

Figure 6 140mm 500dpi
Click here to download high resolution image

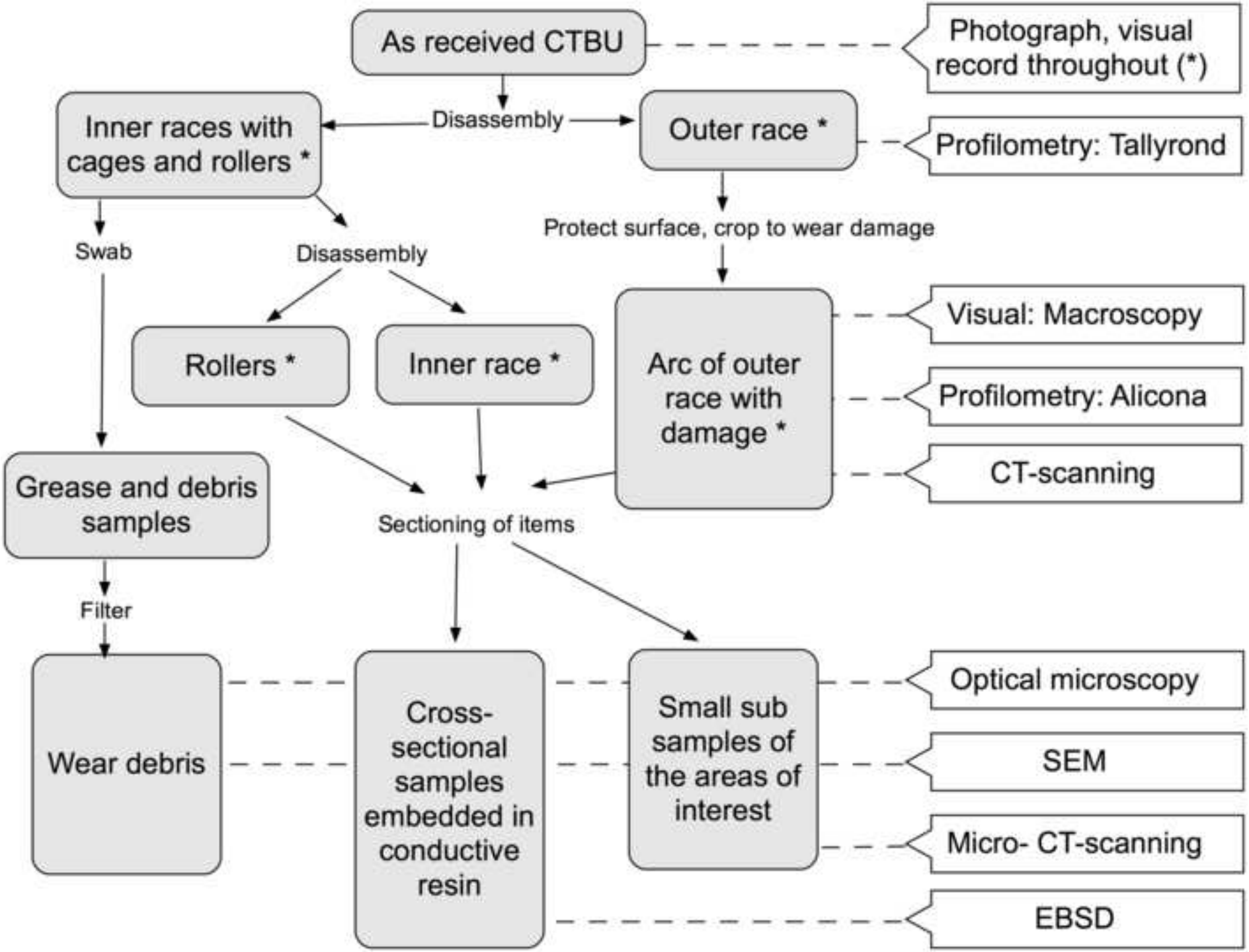

Figure 7 90mm 500dpi
Click here to download high resolution image

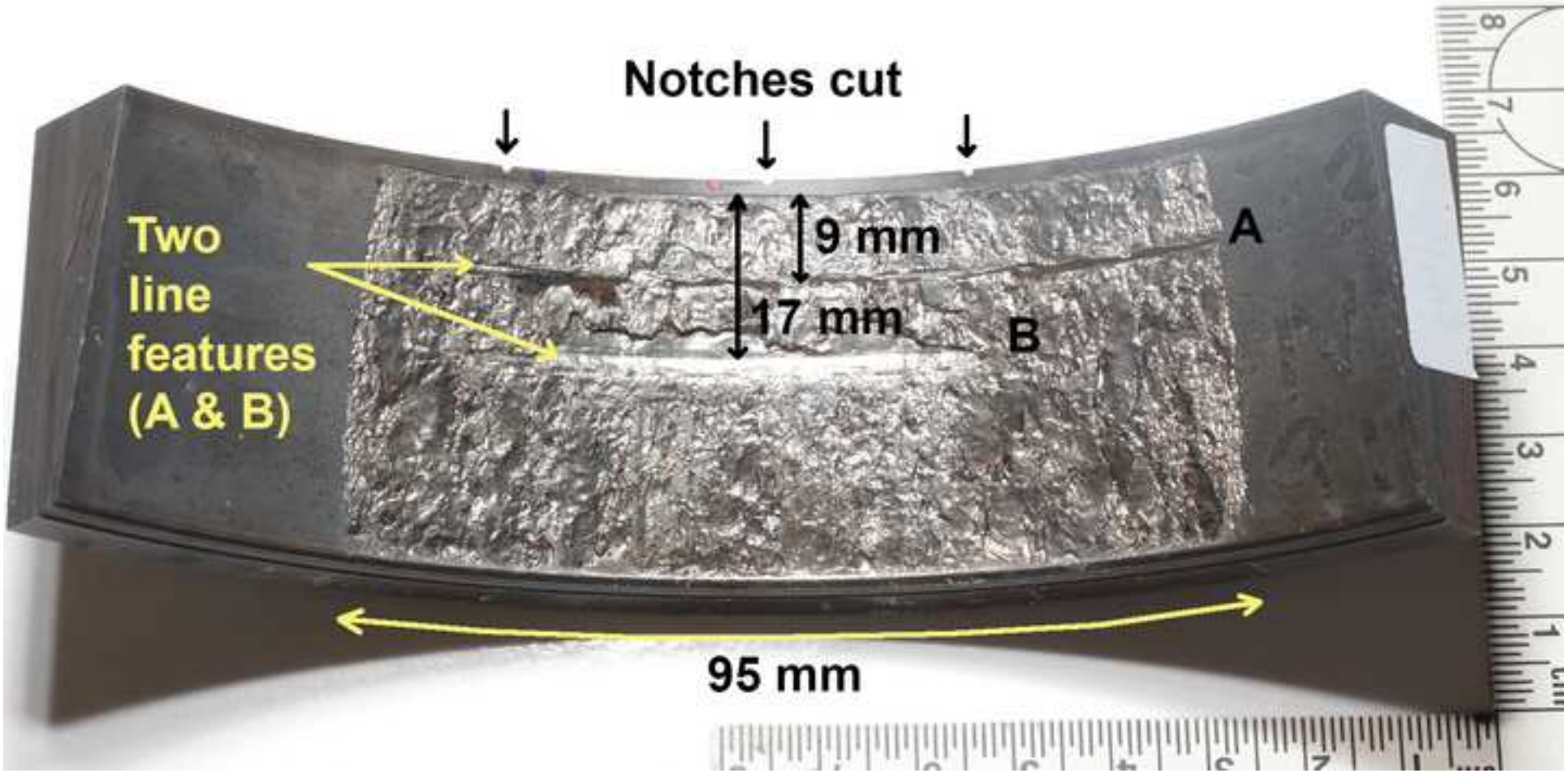

Figure 8 140mm 500dpi
Click here to download high resolution image

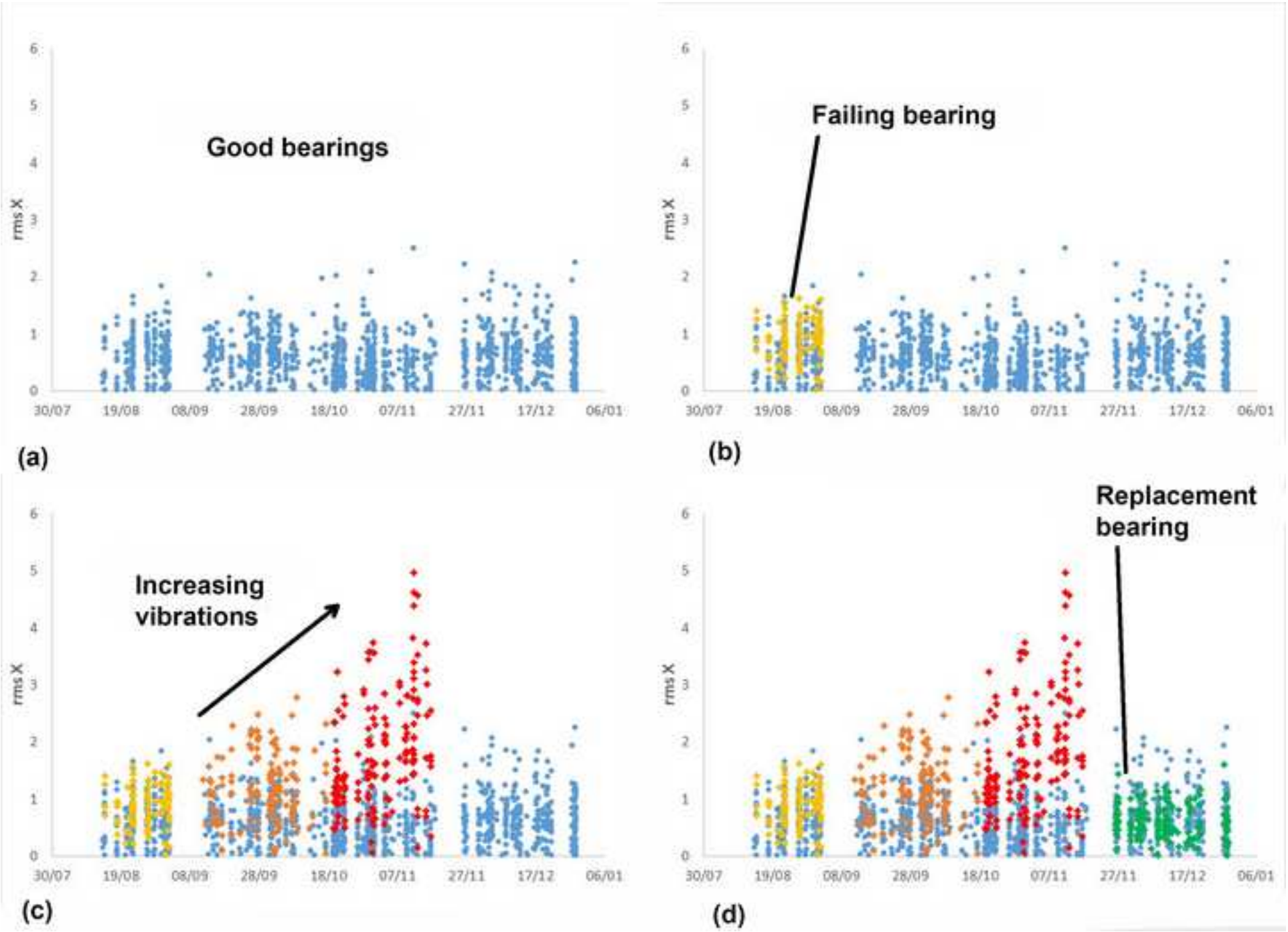

Figure 9 90mm 500dpi
Click here to download high resolution image

Figure 10 excel graph

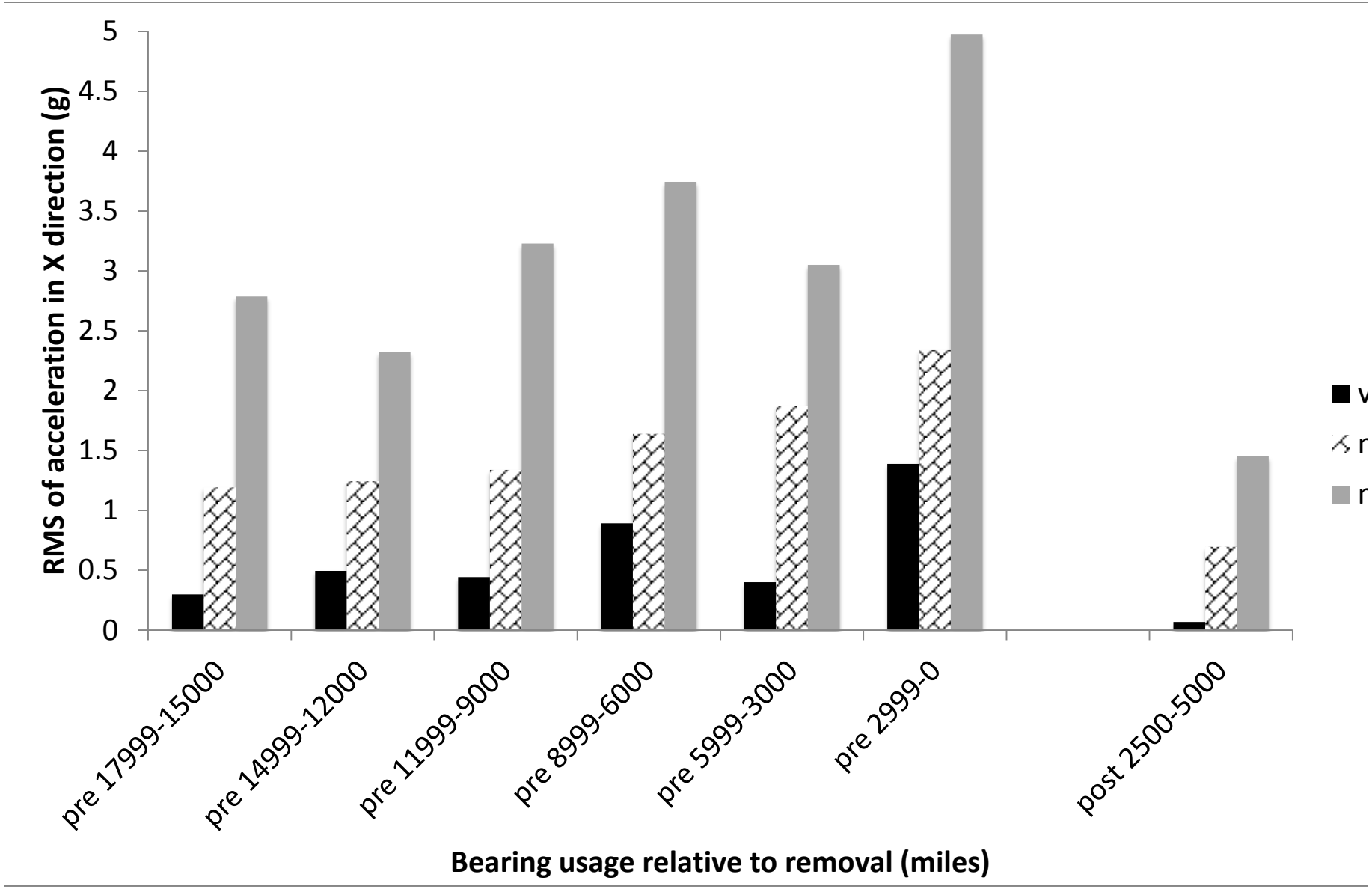

Figure 11 90mm 500dpi
Click here to download high resolution image

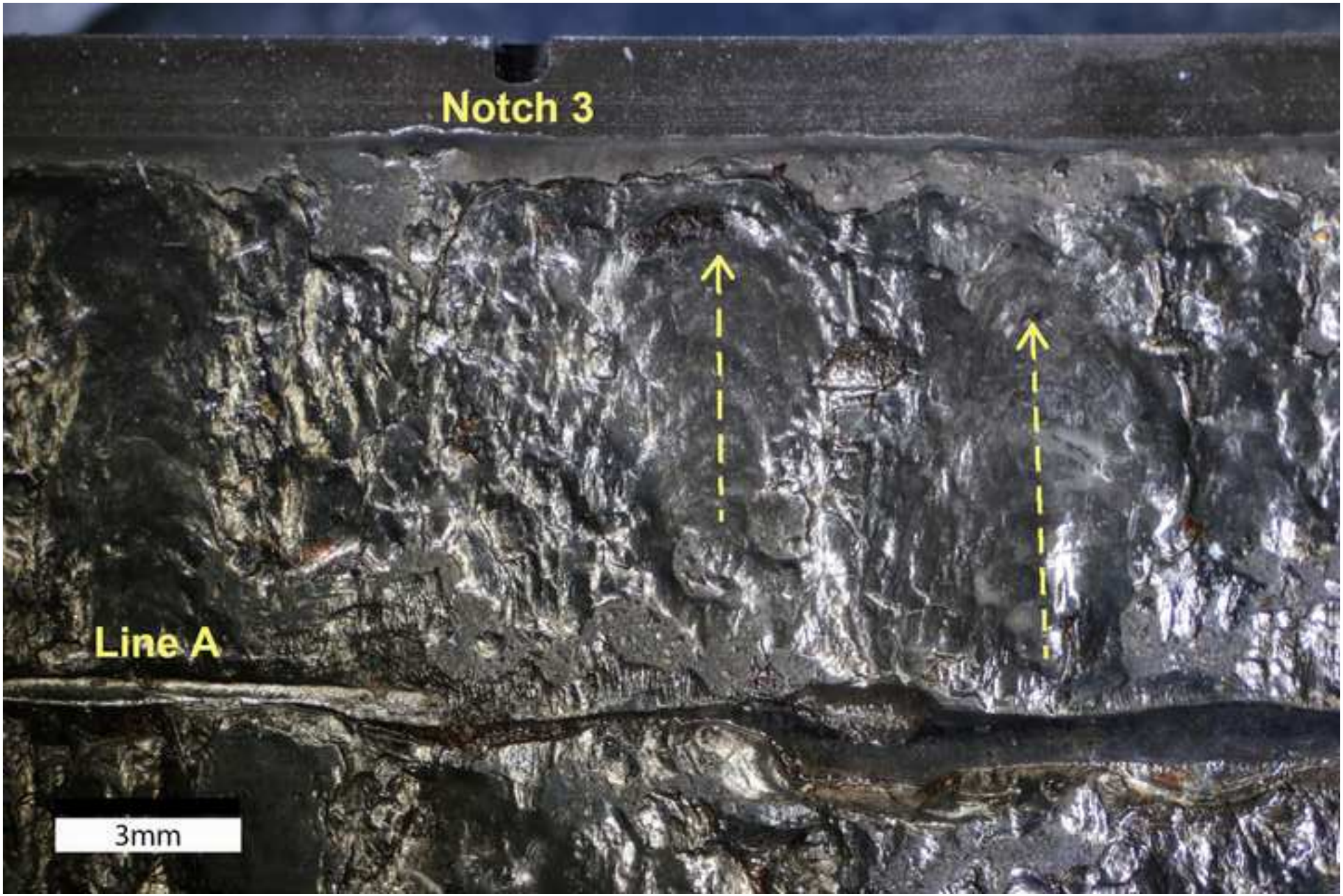

Figure 12 90mm 500dpi
Click here to download high resolution image

Figure 13 90mm 500dpi
Click here to download high resolution image

Figure 14 140mm 500dpi
Click here to download high resolution image

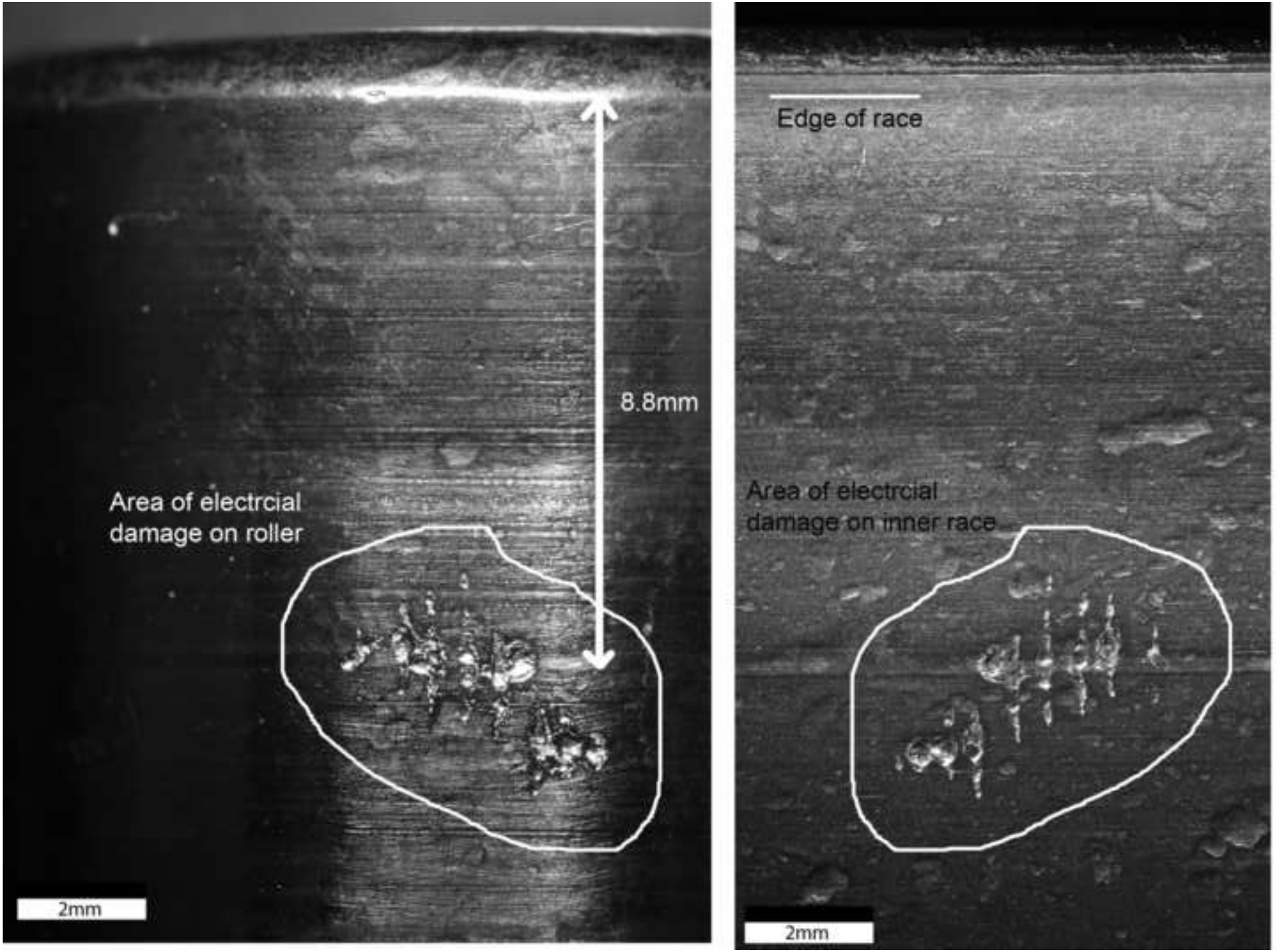

Figure 15 140mm 500dpi
Click here to download high resolution image

Figure 16 140mm 500dpi
Click here to download high resolution image

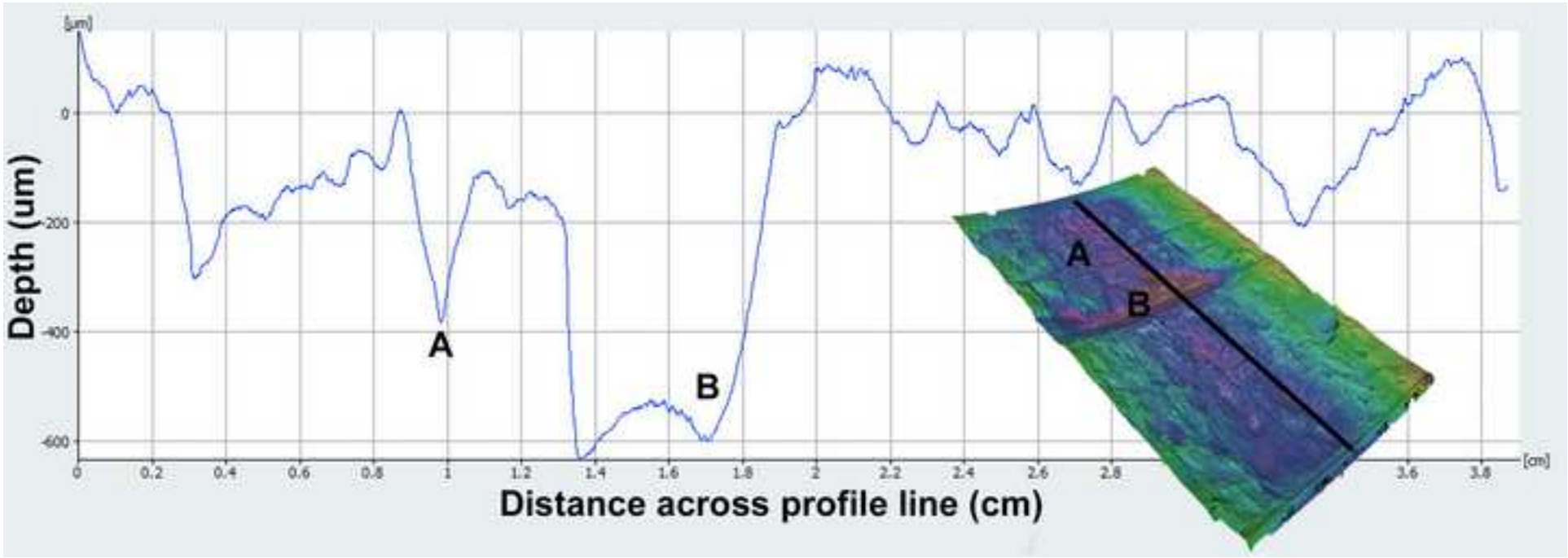

Figure 17 90mm 500dpi
Click here to download high resolution image

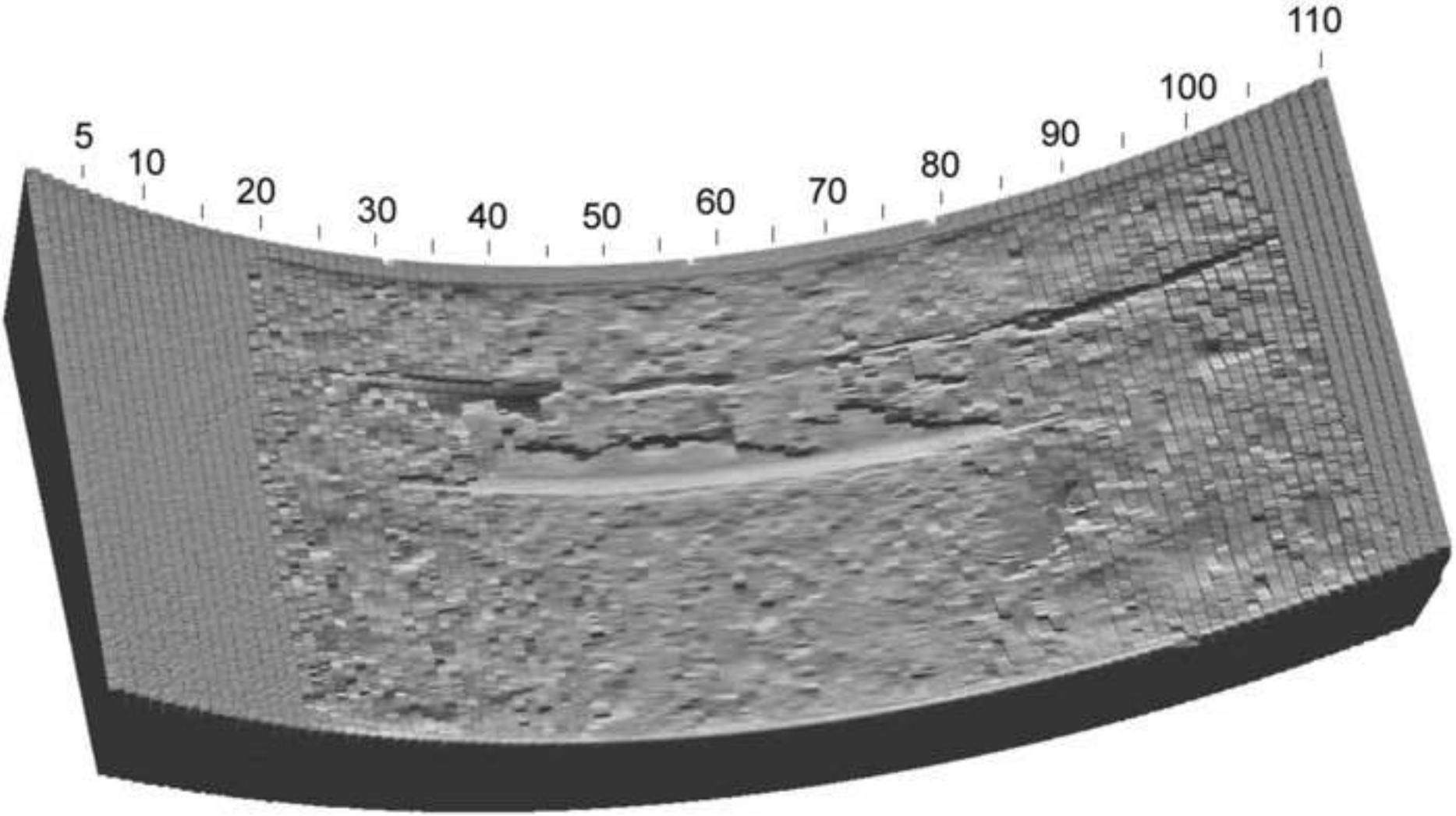

Figure 18 90mm 500dpi
Click here to download high resolution image

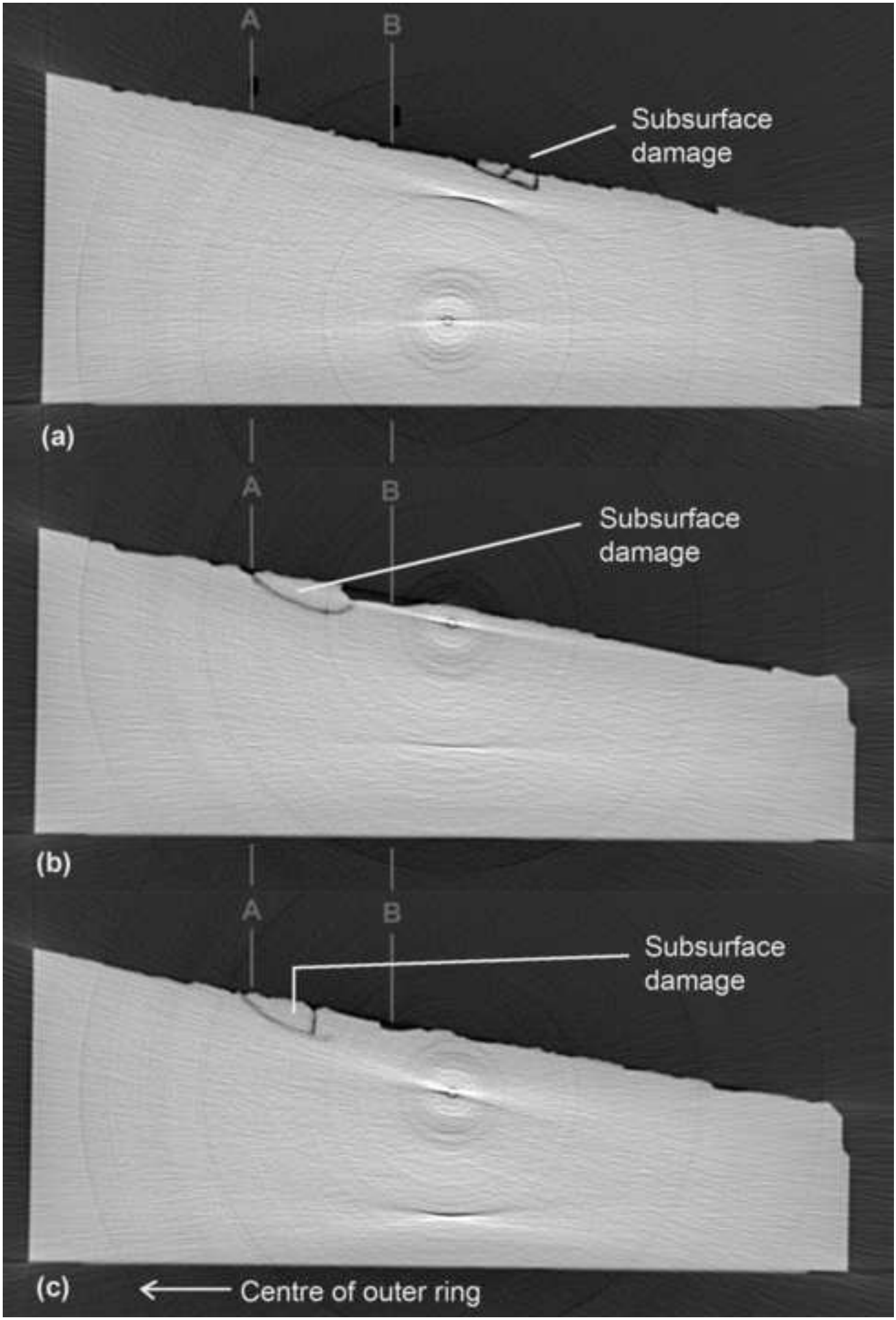

Figure 19 excel graph

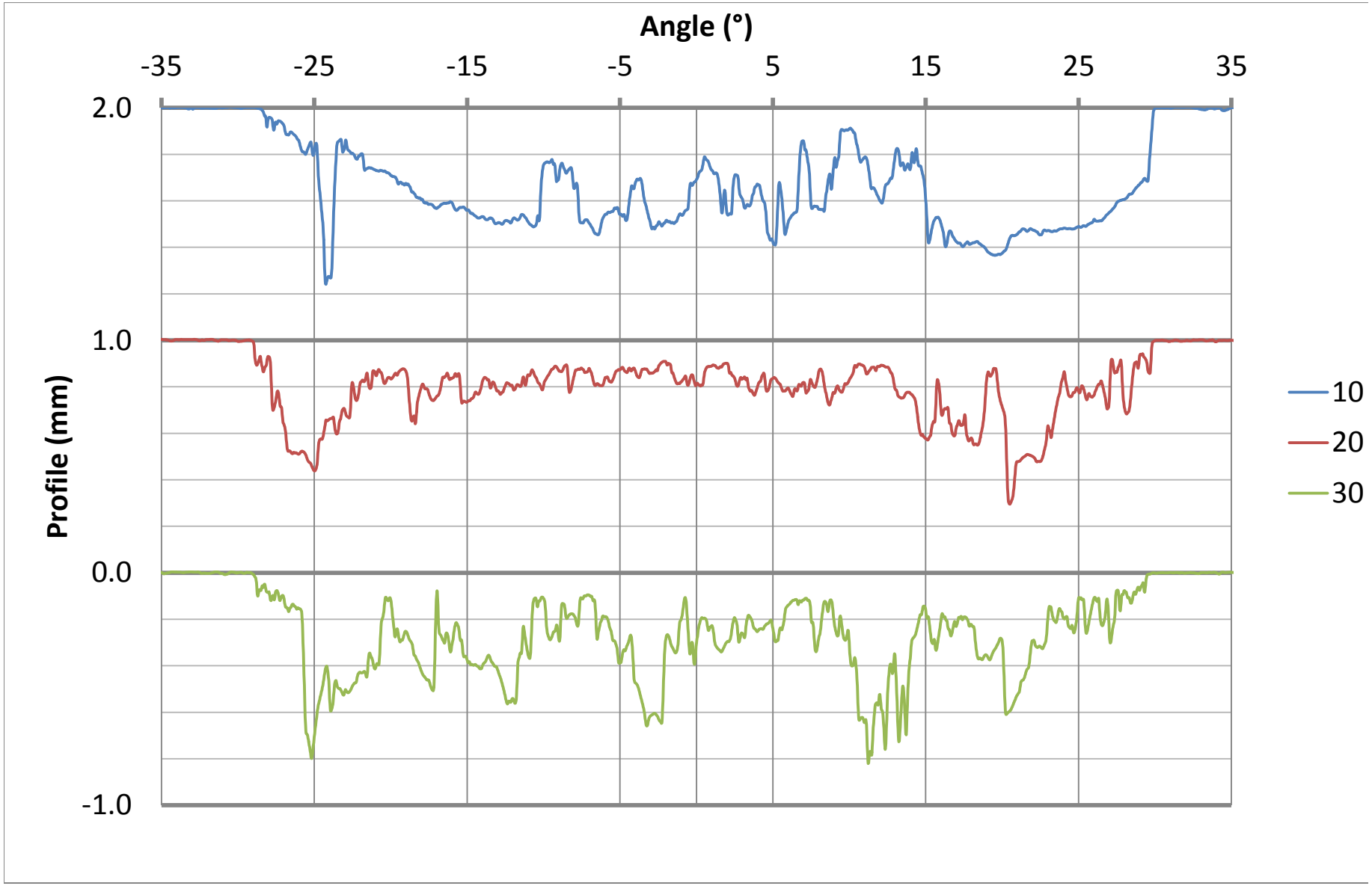

Figure 20 excel graph

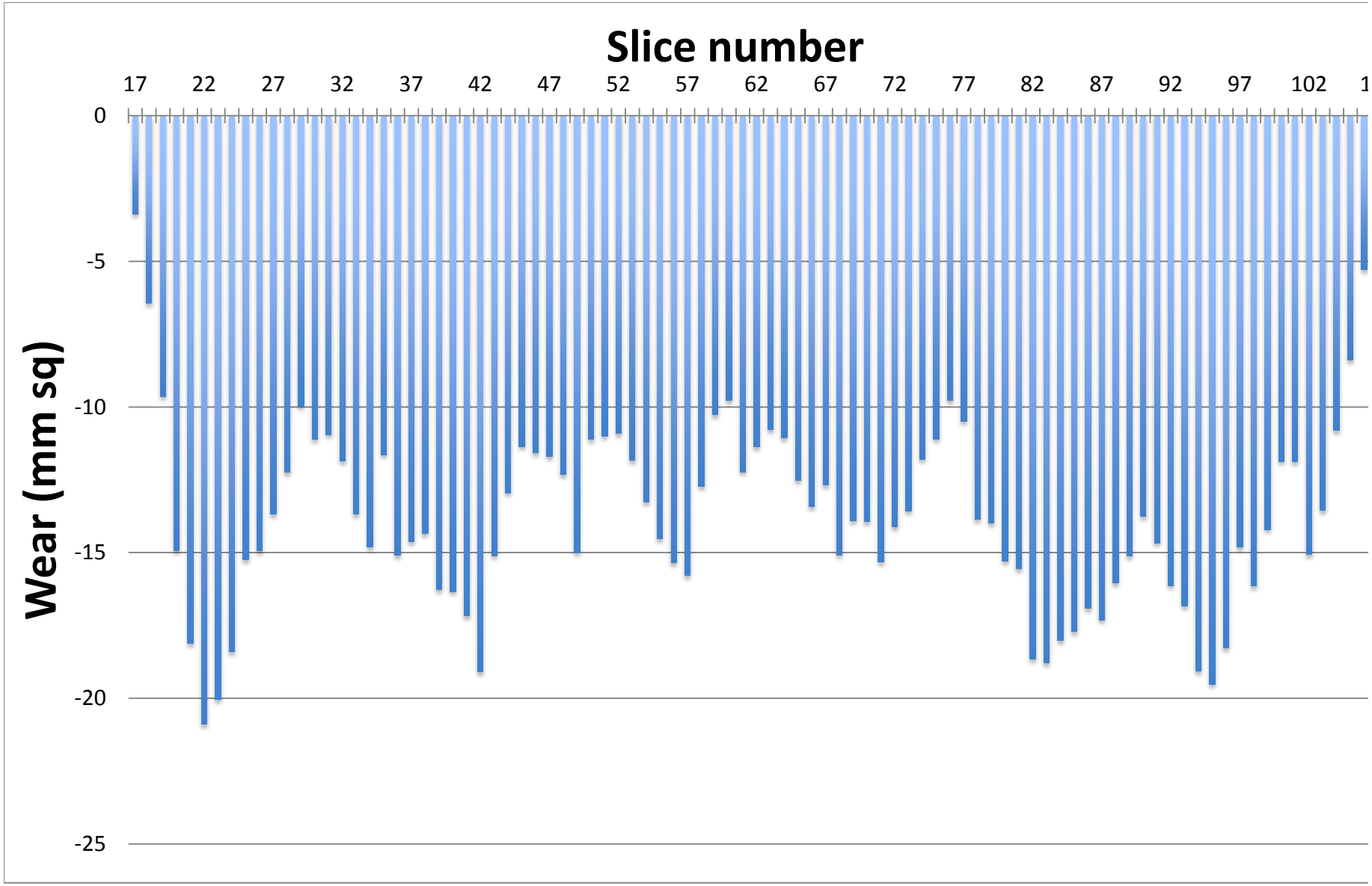

Figure 21 90mm 500dpi
Click here to download high resolution image

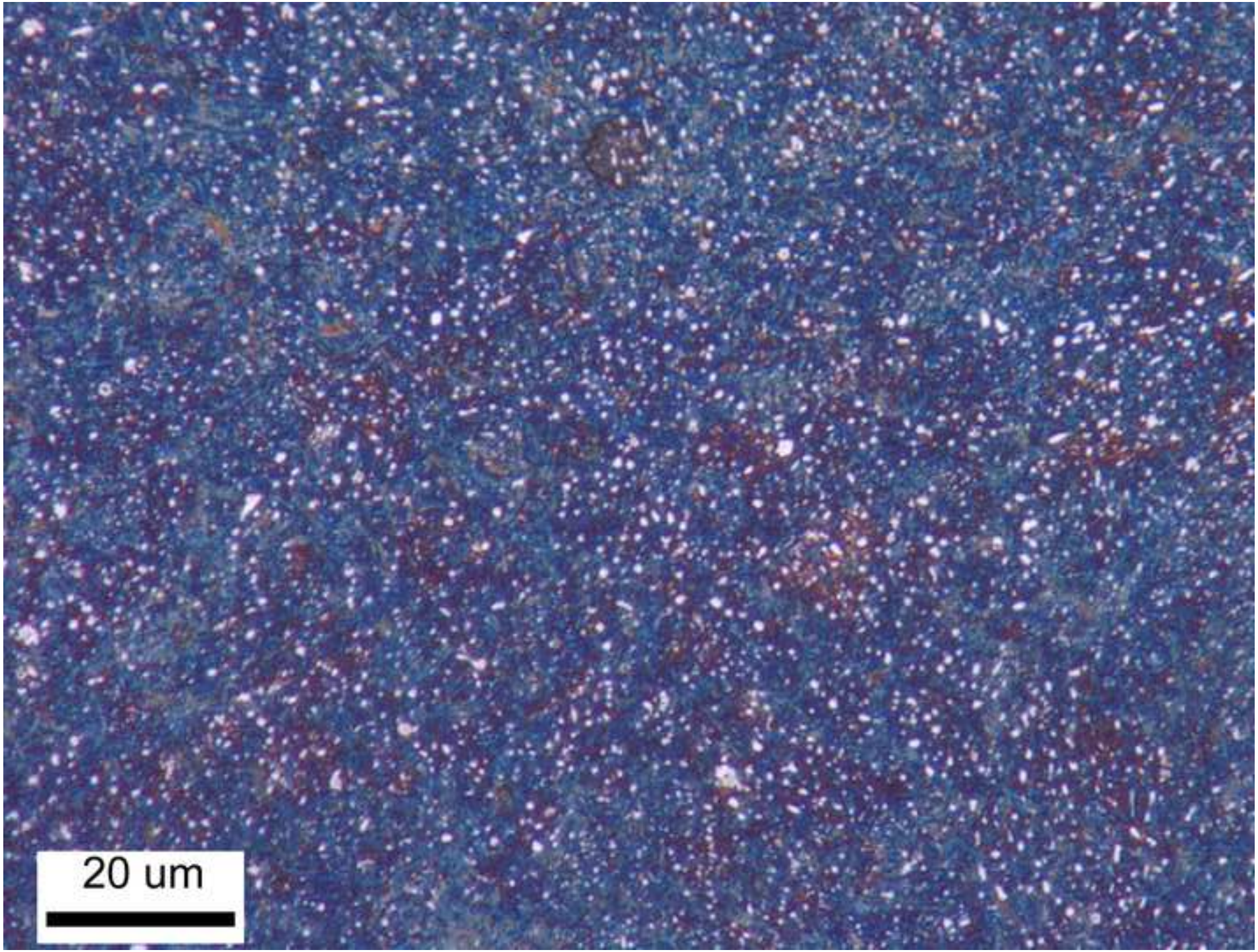

Figure 22 90mm 500dpi
Click here to download high resolution image

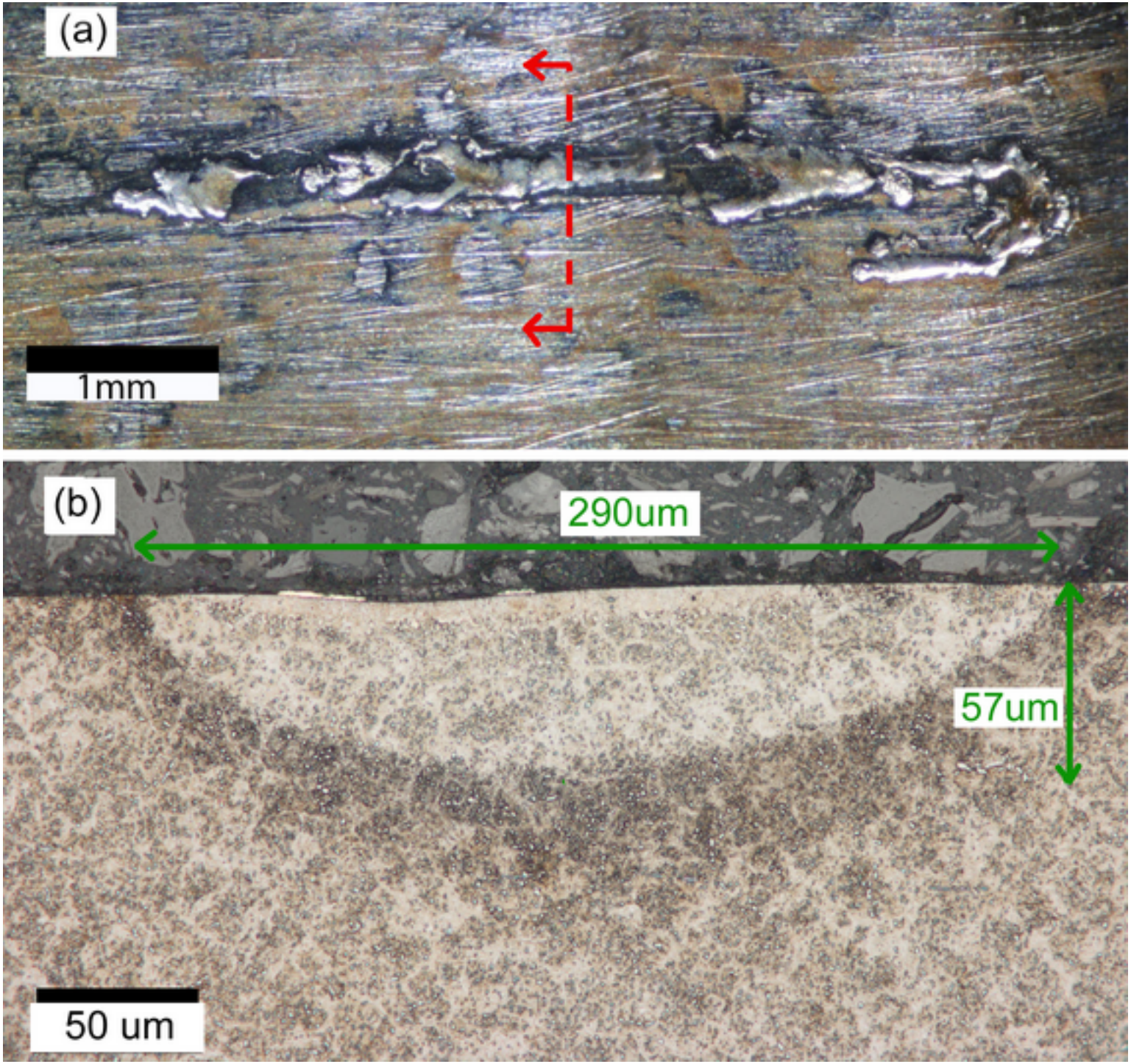

Figure 23 140mm 300dpi
Click here to download high resolution image

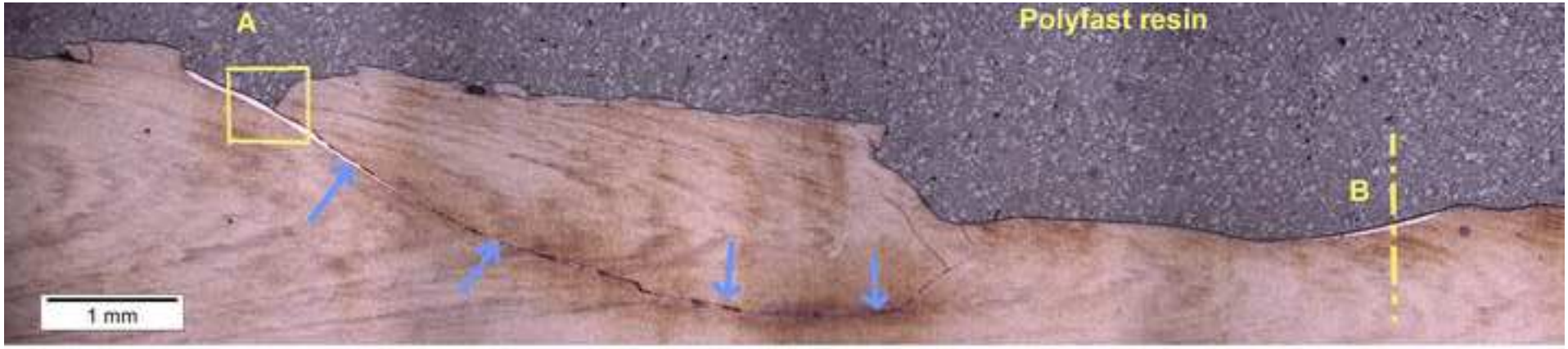

(a)

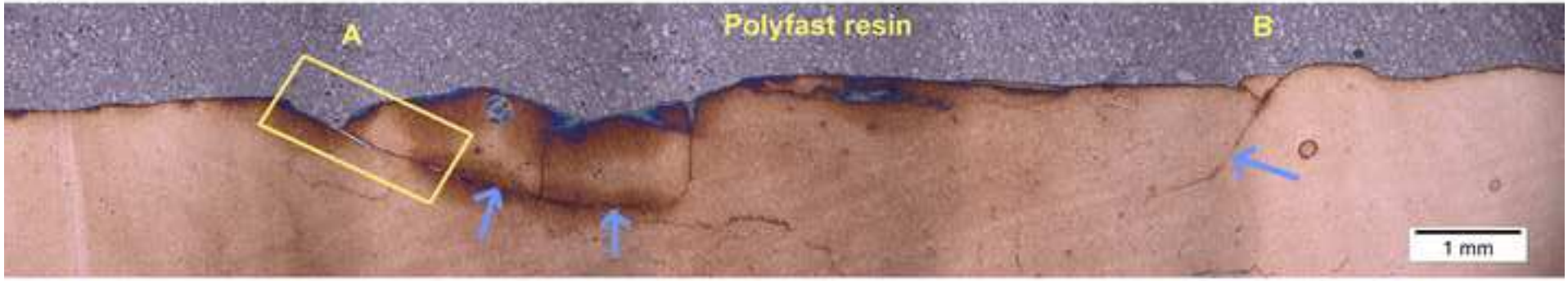

(b)

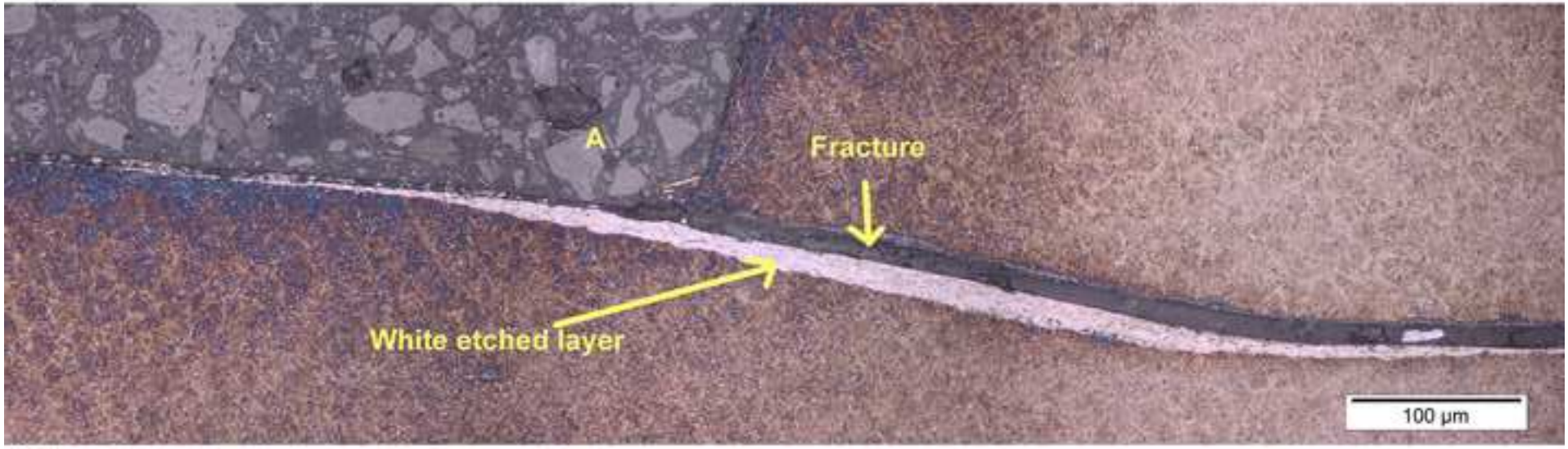

(c)

Figure 24 90mm 500dpi
Click here to download high resolution image

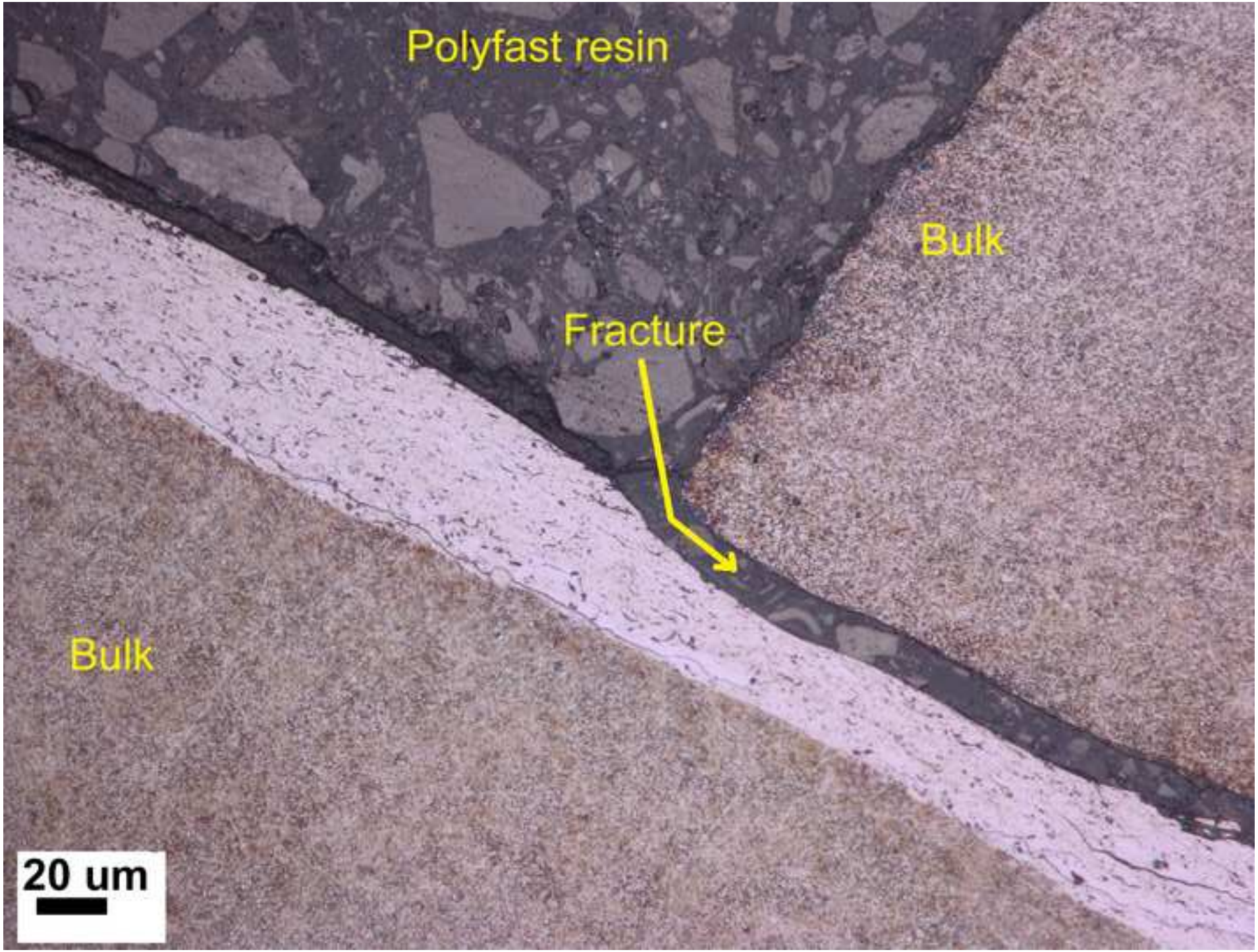

Figure 25 90mm 500dpi
Click here to download high resolution image

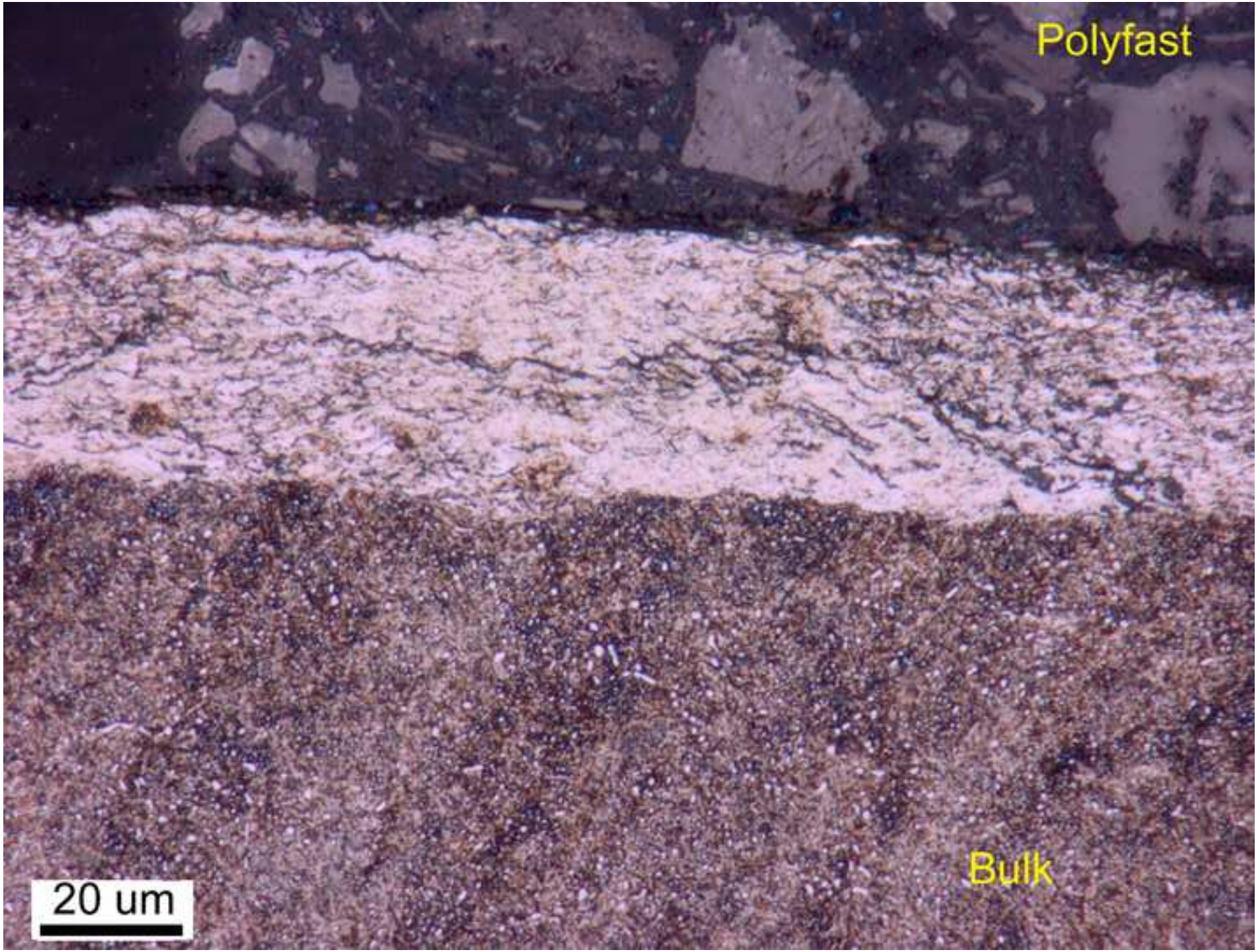

Figure 26 90mm 500dpi
Click here to download high resolution image

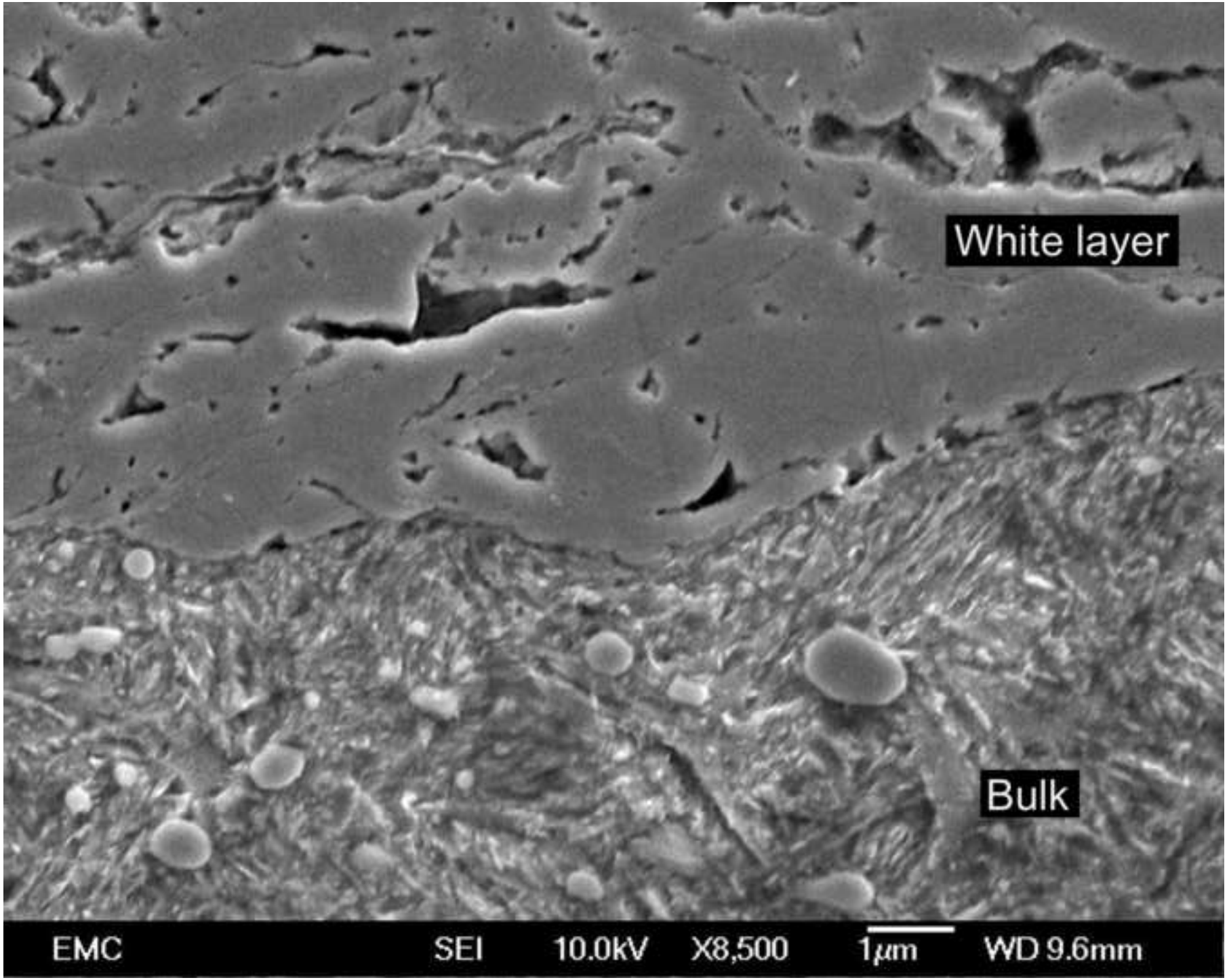

Figure 27 90mm 500dpi
Click here to download high resolution image

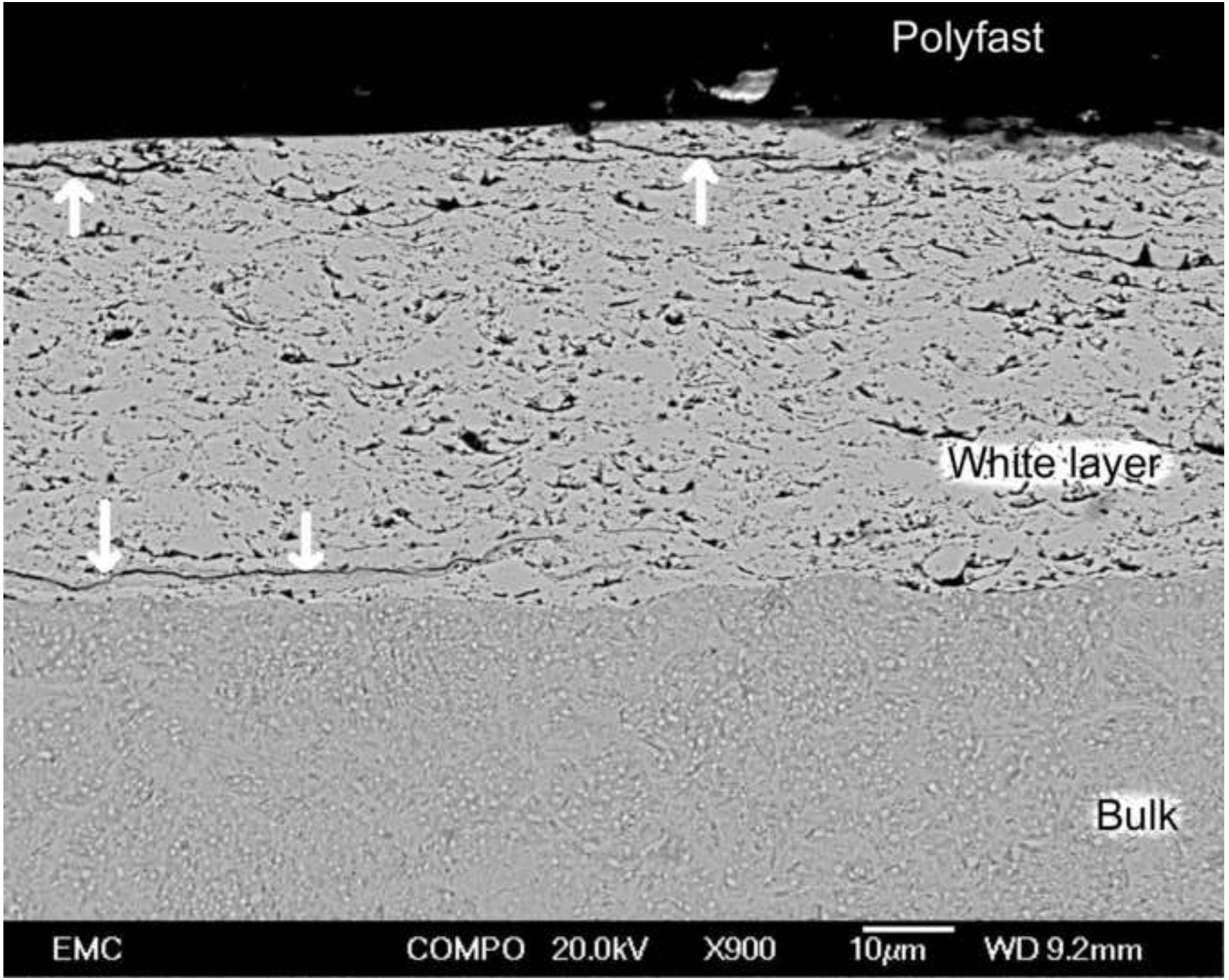

Figure 28 90mm 500dpi
Click here to download high resolution image

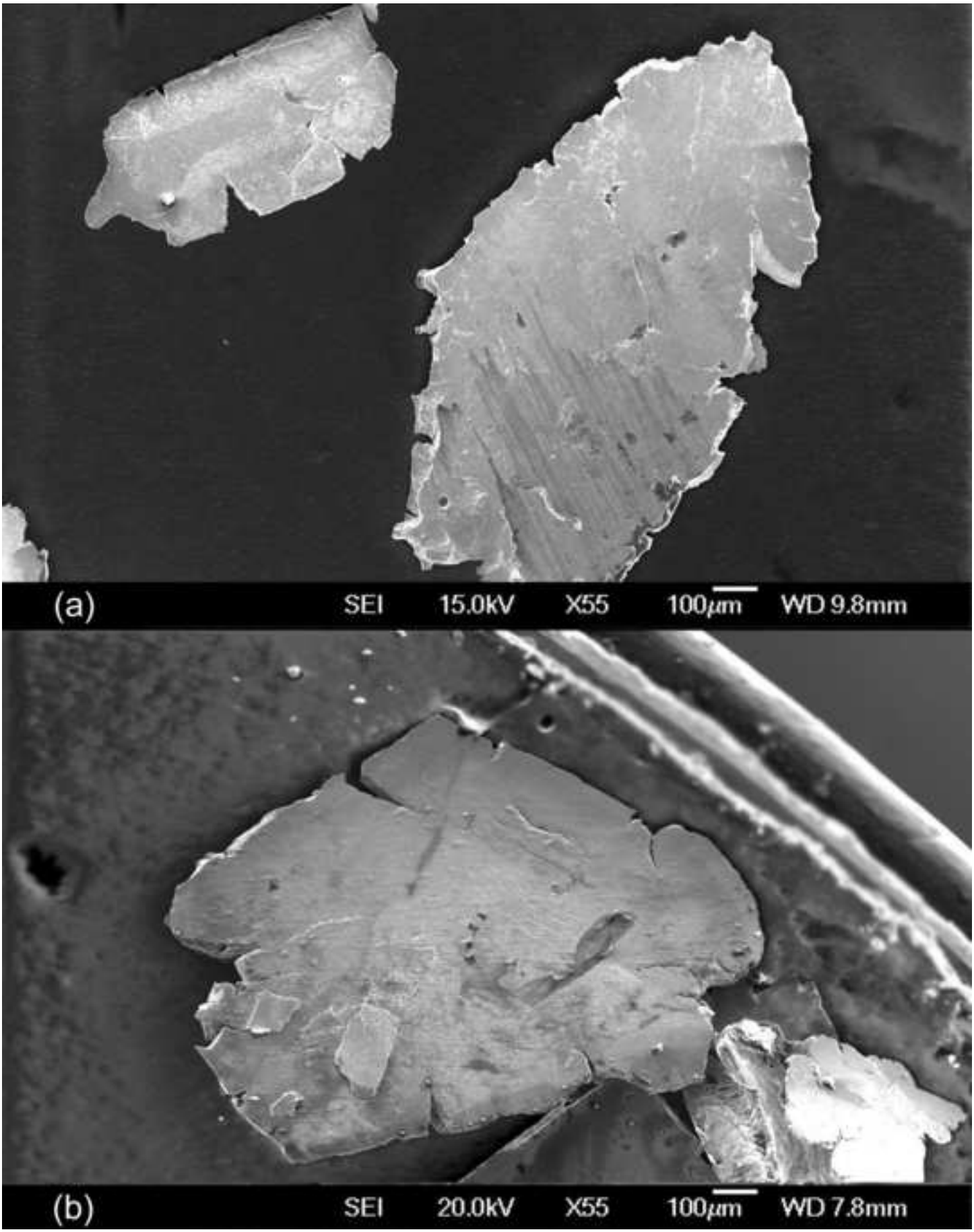

Figure 29 140mm 500dpi
Click here to download high resolution image